

Deformation and Instability Properties of Cemented Gangue Backfill Column under Step-By-Step Load in Constructional Backfill Mining

Yuxia Guo (✉ gyx771221@163.com)

Taiyuan University of Technology

Hongyu Ran

Taiyuan University of Technology

Guorui Feng

Taiyuan University of Technology

Xianjie Du

Taiyuan University of Technology

Yonghui Zhao

Taiyuan University of Technology

Wenshuo Xie

Taiyuan University of Technology

Research Article

Keywords: Cemented gangue backfill column, step-by-step load, deformation, instability, nonlinear creep constitutive model

Posted Date: June 14th, 2021

DOI: <https://doi.org/10.21203/rs.3.rs-335036/v1>

License: © ⓘ This work is licensed under a Creative Commons Attribution 4.0 International License.

[Read Full License](#)

Version of Record: A version of this preprint was published at Environmental Science and Pollution Research on August 9th, 2021. See the published version at <https://doi.org/10.1007/s11356-021-15638-z>.

1 **Deformation and instability properties of cemented gangue backfill column** 2 **under step-by-step load in constructional backfill mining**

3 Yuxia Guo^{1,2*}, Hongyu Ran^{1,2}, Guorui Feng^{1,2**}, Xianjie Du^{1,2}, Yonghui Zhao^{1,2}, Wenshuo Xie^{1,2}

4 ¹ College of Mining Engineering, Taiyuan University of Technology, Taiyuan 030024, China.

5 ² Shanxi Province Research Centre of Green Mining Engineering Technology, Taiyuan 030024, China.

6 *Corresponding author. +86 13653519512 E-mail address: gyx771221@163.com

7 **Abstract:** Constructional backfill mining with cemented gangue backfill column can solve
8 the environmental issues caused by mining activities and the accumulation of waste gangue at
9 a low cost. To study the deformation and instability properties of cemented gangue backfill
10 columns during the advancement of coal mining face, five step-by-step loading paths were
11 adapted to mimic the different loading processes of the roof. The lateral deformation at different
12 heights and axial deformation of the sample were monitored. The results show that the
13 deformation and instability of the backfill column have the properties of loading paths and are
14 affected by the step-by-step loading path. When stress-strength ratio (SSR) is less than 0.6, the
15 lateral of backfill column shrinks during the creeping process. In high-stress levels, lateral creep
16 strain develops faster than axial creep strain. The backfill column has characteristics of axial
17 creep hardening and lateral creep softening during the step-by-step loading process. The
18 instantaneous deformation modulus and instantaneous Poisson's ratio show an upward trend.
19 The bearing capacity of backfill column under the step-by-step load is related to loading paths
20 and is no less than uniaxial compressive strength. The non-uniformity of the lateral deformation
21 of backfill column leads to excessive localized deformation that mainly occurs in the middle,
22 causing the overall instability. The development of cracks of backfill column under step-by-
23 step load could be divided into 4 stages according to SSR. Under different step-by-step loading
24 paths, the axial creep strain rate is nearly a constant before entering the accelerated creep stage.
25 A nonlinear creep constitutive model with a creep strain rate trigger was proposed to depict the
26 development of axial strain under step-by-step load. This research will provide a scientific
27 reference for the design of the advancing distance and cycle for the hydraulic support, and
28 reinforcement of the backfill column.

29 **Keywords:** Cemented gangue backfill column; step-by-step load; deformation; instability;
30 nonlinear creep constitutive model

31 **1 Introduction**

32 Cemented gangue backfill mining technology is an important part of the “green mining”
33 system for coal mining, it not only controls the movement of the overlying strata and the surface
34 subsidence effectively, but also consumes a large amount of coal gangue (Chen et al. 2016a).
35 The material used for coal mine backfill mining is made of coal gangue, cement, fly ash, and
36 water. Generally, the method of full backfilling is used in coal mining, that is, all mined-out
37 space is filled with cemented gangue backfill material. However, the cost of cement and fly ash
38 is relatively high, and the production of coal gangue only accounts for about 20% of the output
39 of raw coal (Liu et al. 2020). The high cost and limited raw materials impede the promotion of
40 coal mine full backfill mining; thus, partial backfill mining (Zhu et al. 2017) and constructional
41 backfill mining (Feng et al. 2019; Du et al. 2018) are proposed, and the roof is supported by
42 strip and column backfill bodies (Zhu et al. 2017; Wang et al. 2019a), as shown in Fig. 1. The
43 support of the unconfined backfill columns can improve the stress state of the surrounding rock
44 in the goaf, maintaining the stability of the mined-out area and controlling surface subsidence,
45 and forming a large amount of underground space that can be used for other purposes such as
46 underground reservoir (Feng et al. 2019; Du et al. 2019a). During the advancing process of the
47 coal mining face, the pressure applied on the unconfined columns increases gradually as the
48 advancement of hydraulic supports step-by-step (Zhang et al. 2017). Therefore, the deformation
49 and mechanic responses of the backfill column under the step-by-step load are closely related
50 to the stability of the goaf. It is necessary to study the stability of the backfill column under the
51 step-by-step load to ensure the safety of workers during the mining process.

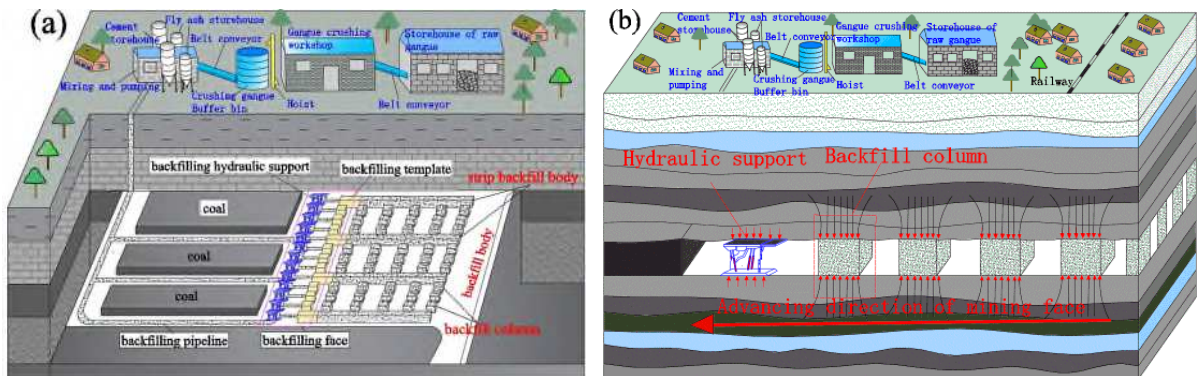
52 Many scholars have carried out a series of studies on the mechanics and deformation
53 characteristics of cemented gangue backfill material (Du et al 2018; Du et al. 2019a). The
54 mechanic and deformation properties of cemented paste backfill (CPB) are affected by external
55 conditions. The main considerations are the use of stirrups (Du et al. 2019b); the loading method
56 (uniaxial compression and triaxial compression) (Fall et al. 2007); the different temperature and

57 sulphate environment (Fall et al. 2010); the structural factors (filling time, interval, and surface
58 angle) and loading rate effect (Cao et al. 2017; Cao et al. 2019); the particle size distribution of
59 aggregates (Wu et al. 2021a); interface angles between rock and backfill (Yin et al. 2021);
60 curing temperature and silica fume (Xu et al. 2020); curing under stress (Yilmaz et al. 2014;
61 Guo et al. 2020); under triaxial cyclic loading and unloading (Wang et al. 2019b); mixing
62 method of raw material (Sun et al. 2019b); and dynamic loading (Li et al. 2020). Except for the
63 external factors, the proportion of raw material and additions can also affect the deformation
64 and mechanical properties of CPB (Liu et al. 2019; Qi et al. 2015; Chen et al. 2020). However,
65 none of the above studies involve step-by-step load.

66 The instability of the backfill body does not happen immediately but occurs gradually over
67 time, the creep characteristics of the backfill body and the stability of the goaf are closely related.
68 The creep properties of cemented gangue backfill material under uniaxial compression and
69 triaxial compression were investigated (Wu et al. 2021b). Cemented gangue backfill is a visco-
70 elastoplastic material with obvious rheological properties, and the disturbance will accelerate
71 the creep process of the backfill body (Sun et al. 2018). Besides, the cemented gangue backfill
72 has creep hardening characteristics, and the creep hardening mechanism and the creep
73 properties under high-stress areas are explored (Chen et al. 2016b; Ran et al. 2021). The triaxial
74 creep properties of cemented gangue-fly ash backfill under seepage-stress coupling were also
75 tested (Hou et al. 2020). The above studies only focused on the axial creep deformation of the
76 backfill body and did not consider the lateral deformation characteristics. However, many
77 researchers have found that the lateral creep of the rock shows obvious anisotropy and has a
78 significantly accelerated stage, and it appears earlier than the axial accelerated creep stage (Fu
79 et al. 2007; Fan et al. 2005). Besides, since the lateral deformation of the backfill body restricts
80 the lateral deformation of the surrounding rock, the backfill body and the surrounding rock
81 share the load, especially when the backfill column is used to strengthen the stability of the coal
82 pillar (Hou et al. 2019; Qi et al. 2019; Yin et al. 2020). Therefore, it is necessary to study the
83 lateral deformation of the unconfined cemented gangue backfill column.

84 As shown in Fig. 1, the backfill columns in the goaf bear the vertical load from the roof,

85 and the pressure increases step by step with the advancement of the coal mining face (Zhang et
 86 al. 2017). When the hydraulic support advances, the load from the roof will increase
 87 accordingly; however, when the hydraulic support stops, the load applied to the columns will
 88 be nearly constant. The deformation and instability characteristics of the backfill column under
 89 this step-by-step loading condition are important physical properties of the constructional
 90 backfill mining, and the step-by-step load is also a method used for rock creep tests (Fu et al.
 91 2007; Fan et al. 2005; Shi et al. 2019; Jia et al. 2018; Wu et al. 2018). In addition, due to the
 92 influence of factors such as the advancing speed of the coal mining face and the facilities
 93 maintenance, the moving distance and cycle of the hydraulic support are different. Therefore,
 94 the step-by-step loading increment exerted to the backfill columns is different, and it is not all
 95 uniform. In this study, the axial and lateral deformation characteristics and bearing capacity of
 96 test samples under five step-by-step loading paths are analyzed, the axial nonlinear creep
 97 constitutive model is established, and the instability mechanism of the backfill column is
 98 discussed. This research could provide a scientific reference for the advancing distance and
 99 cycle of the hydraulic support, and reinforcement of the backfill column.



100
 101 **Fig. 1.** Schematic diagram of the unconfined backfill columns in constructional backfill mining: (a) layout of the
 102 unconfined backfill column, (b) load on the unconfined backfill column.

103 2 Material and methods

104 2.1 Sample preparation

105 Cemented gangue backfill material (CGBM) is a paste-like material made of ordinary
 106 Portland cement (190 Kg/m³) Type 42.5, secondary fly ash (380 Kg/m³), coal gangue (950
 107 Kg/m³), and tap water (350 Kg/m³) (Du et al. 2019; Qi et al. 2015; Wang et al 2021; Wang et
 108 al. 2020). Fly ash is sampled from thermal power plant of the Fenxi mining group. Coal gangue

109 was collected from gangue mountain of Tunlan colliery located in Shanxi province of China.
 110 The crushed coal gangue was divided into three groups (0–5 mm, 5–10 mm, and 10–15 mm)
 111 according to the nominal diameter, which accounted for 30%, 35%, and 35%, respectively, of
 112 the total aggregate mass (Wang et al. 2020). The morphology of raw materials and test samples
 113 are shown in Fig. 2. The fineness module of the fine aggregate (0–5 mm) was 3.10. The moisture
 114 content and specific gravity of coal gangue aggregate were tested, by 0.74 % and 2.3 g/cm³,
 115 respectively. Table 1 shows the physical properties and chemical components of cement and fly
 116 ash. Fig. 3 presents the particle size distribution of coal gangue and fly ash. The Φ 50×100 mm
 117 mold was used to cast the test samples (Chen et al. 2016b; Sun et al 2018). Samples were
 118 removed from the molds after casting for 24 h, and then it was placed in a standard curing room
 119 for 28 d (Sun et al 2018). The end faces of the test samples were polished to meet the
 120 dimensional requirement and the smoothness requirement of the international rock mechanics
 121 test standard.

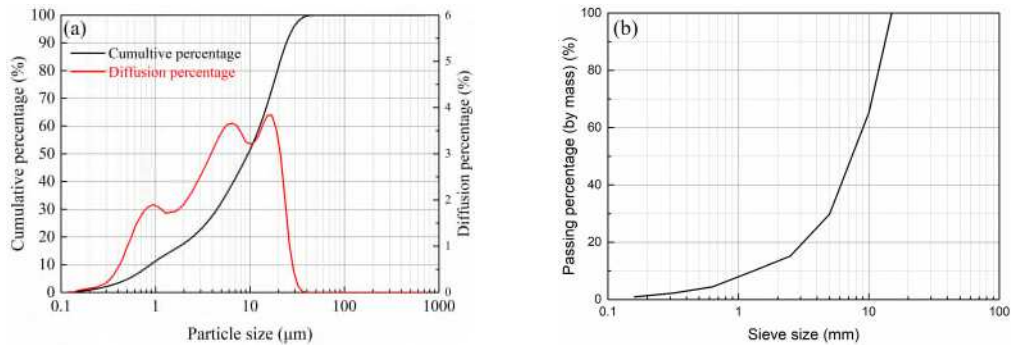


122 **Fig. 2.** Morphology of raw material and test samples.

123 **Table 1** Chemical components and physical properties of fly ash and cement.

124

| | | Fly ash | Cement |
|---------------------|--|---------|--------|
| Chemical components | SiO ₂ | 52.42% | 22.36% |
| | Al ₂ O ₃ | 32.48% | 5.53% |
| | Fe ₂ O ₃ | 3.62% | 3.45% |
| | CaO | 3.05% | 65.08% |
| | MgO | 1.01% | 1.27% |
| | TiO ₂ | 1.26% | - |
| Physical properties | Specific gravity [g/cm ³] | 2.2 | 3.1 |
| | Specific surface [m ² / kg] | 415 | 349 |
| | Fineness (>45μm) [%] | 42.54 | 5 |
| | Moisture content [%] | 0.56 | - |



125
126 **Fig. 3.** Particle size distribution of fly ash (a) and coal gangue aggregate (b).

127 **2.2 Experimental test protocol**

128 To simulate the process of applying the pressure to the backfill columns by the roof, the
129 step-by-step loading test was carried out on the ETM-205D computer-controlled
130 electromechanical testing machine. The pressure head of the press moves from top to bottom,
131 which can conduct two loading methods of force loading and displacement loading, and can
132 perform a uniaxial compressive creep test. After 28 d of curing, the ultrasonic pulse velocity of
133 the specimens was tested by an NM-4B nonmetal ultrasonic instrument, and the specimens with
134 a P-wave velocity of 2.5 ± 0.05 Km/s were selected for the tests.

135 **2.2.1 Deformation monitoring**

136 The TST3822E-20 static resistance strain equipment was used to monitor the axial and
137 lateral strain of the specimen. As shown in Fig. 4, the strain gauges were vertically distributed
138 along with the axial and lateral directions on the specimen surface. To distinguish the position
139 of the strain gauges, L and R represent the left side and right side of the sample, respectively.
140 The axial strain gauges were attached to the middle of the specimen, and three radial strain
141 gauges were arranged at equal intervals (Li et al. 2020). To monitor the deformation at various
142 positions, eight strain gauges were symmetrically stuck on the specimen, and the length of the
143 strain gauge (20×4 mm) was greater than the maximum particle size of the aggregate.

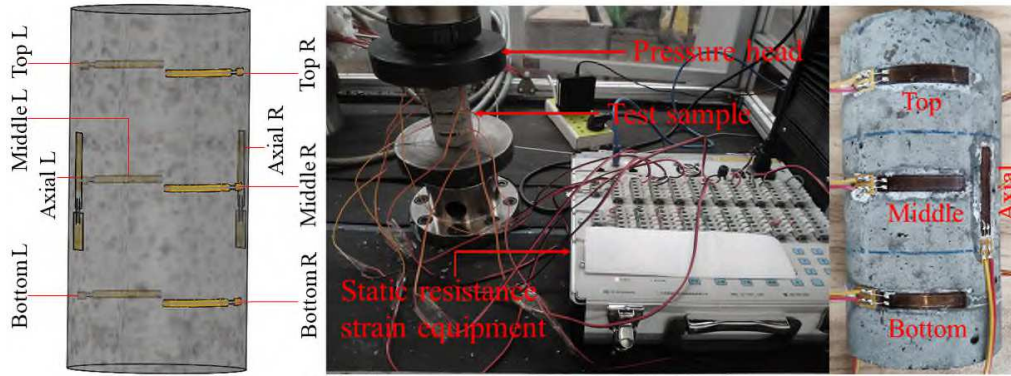


Fig. 4. Testing machine and the distribution of strain gauges.

144

145

146 2.2.2 Step-by-step loading test

147

148

149

150

151

152

153

154

155

156

157

158

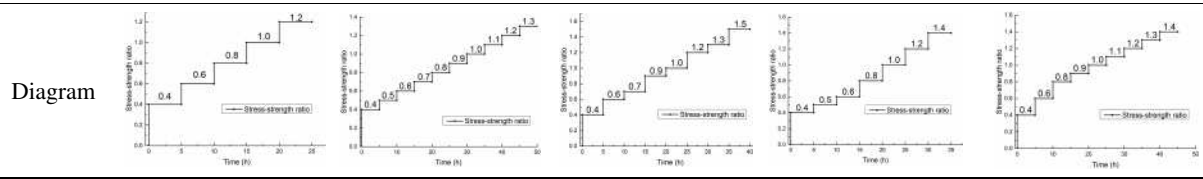
159

160

The displacement loading method was used in the uniaxial compression test and step-by-step loading test, and the loading rate was 0.15 mm/min. The average uniaxial compressive strength (UCS) of the test CGBM samples was 5.05MPa. To realize the different loading paths are exerted to the unconfined backfill column, according to the average UCS, the stress–strength ratio (SSR) growth plan is adopted. The first-level SSR is 40%, and five step-by-step loading paths are designed, as shown in Table 2. The 20% UCS is regarded as a large increment that is used to simulate the long moving distance of the hydraulic support each time, and the 10% UCS is regarded as a small increment that is used to simulate the short moving distance of the hydraulic support each time. According to the literature (Chen et al. 2016b), when the load reached the set value, the pressure is kept constant for 5 h, and the duration of the last step depends on the specific damage of the backfill column until the test sample undergoes creep failure. To avoid the test sample from being completely crushed so that the macro cracks can be seen, the press stops working when the load drops more than 10%.

Table 2 Loading paths of the step-by-step loading creep test.

| | A | B | C | D | E |
|-------|------------------------------|------------------------------|--|---|---|
| Steps | Large increment uniform load | Small increment uniform load | Large increment and small increment alternate load | Small increment uniform load→Large increment uniform load | Large increment uniform load→Small increment uniform load |
| 1 | 40% | 40% | 40% | 40% | 40% |
| 2 | 60% | 50% | 60% | 50% | 60% |
| 3 | 80% | 60% | 70% | 60% | 80% |
| 4 | 100% | 70% | 90% | 80% | 90% |
| 5 | ... | 80% | 100% | 100% | 100% |
| 6 | | 90% | ... | ... | ... |
| 7 | | 100% | | | |

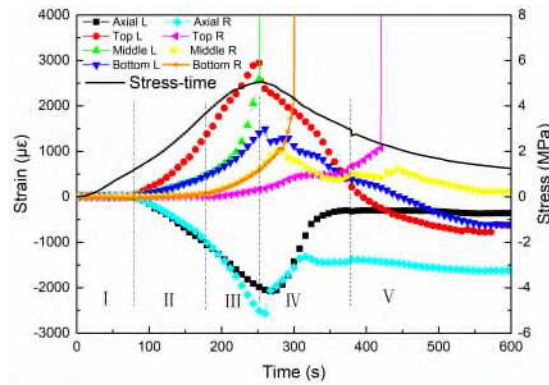


161 3 Results and discussion

162 3.1 Deformation under uniaxial compression test

163 Fig. 5 shows the stress–time curve and strain–time curve of the CGBM specimen in
 164 uniaxial compression. The failure process of the CGBM sample can be divided into five stages:
 165 initial compaction stage, elastic stage, plastic stage, rapid decline stage, and residual bearing
 166 stage. During the initial compaction stage, the stress increased slowly with time, and the
 167 porosity of the CGBM sample was compacted; there is no obvious strain variation in the lateral
 168 direction. The axial strain and lateral strain increased slowly in the elastic stage, and the lateral
 169 expansion of the specimen appeared firstly at the middle and top (the positions of the strain
 170 gauges). During the plastic stage, the lateral strain at the middle and top positions increased
 171 rapidly. In the rapid decline stage and residual bearing stage, the lateral strain at some positions
 172 increased sharply due to the production of macrocracks on the surface, while the lateral strain
 173 at some positions decreased continuously because the strain gauges were separated from the
 174 specimen or the block of the measured part was separated from the main body, which means
 175 that the sample loses its bearing capacity completely.

176 By comparing the lateral strain–time curves at different positions of the test sample, it can
 177 be concluded: the lateral expansion of the test sample under compression was not uniform;
 178 when the test sample was destroyed, the largest lateral deformation occurred at the middle of
 179 the specimen; the rapid growth of lateral localized deformation eventually led to the overall
 180 instability of the specimen (Sun et al. 2019a).

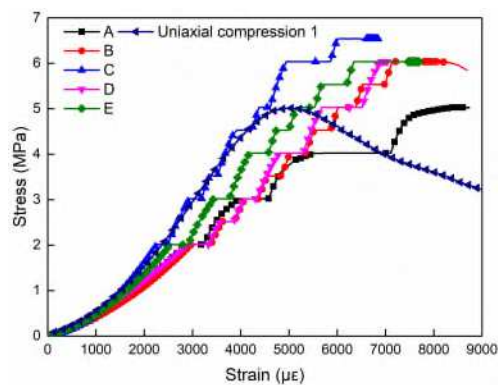


181
182 **Fig. 5.** Strain–time curve and stress–time curve under uniaxial compression.

183 **3.2 Axial deformation under step-by-step load**

184 **3.2.1 Stress-strain curve**

185 Fig. 6 shows the stress–strain curve under the step-by-step load and the uniaxial
186 compression. The axial strain increased with the increase in stress. When the stress increased
187 to the peak value, the strain rate increased suddenly and the specimen was destroyed. Except
188 for group A, the peak stresses under the different step-by-step load paths were significantly
189 greater than the peak stress under the uniaxial compression test. Because of the creep process,
190 the peak strains of the CGBM sample under different step-by-step loading paths were larger
191 than the peak strain under the uniaxial compression. The cemented gangue backfill column
192 showed axial creep hardening characteristic during the step-by-step loading process (Chen et
193 al. 2016b). However, the bearing capacity of the backfill column under the step-by-step load
194 was closely related to the step-by-step loading paths. The ultimate bearing capacity of group A
195 was the same as the average UCS, and the highest UCS was group C, Groups B, D, and E were
196 basically the same. The bearing capacity of backfill column under the step-by-step load is
197 related to loading paths and is no less than UCS.



198
199 **Fig. 6.** Stress–strain curve under step-by-step load and uniaxial compression.

200 3.2.2 Strain–time curve

201 The strain–time curve under step-by-step load is shown in Fig. 7(a). The instantaneous
202 strain and creep strain under various SSRs are shown in Table 3. Specimen A was destroyed
203 during the final-step loading process, specimens B, C, D and E were destroyed in the final creep
204 stage, but specimen D was destroyed after 1 min when the test entered the creep process. The
205 axial deformation of the CGBM sample has the following characteristics:

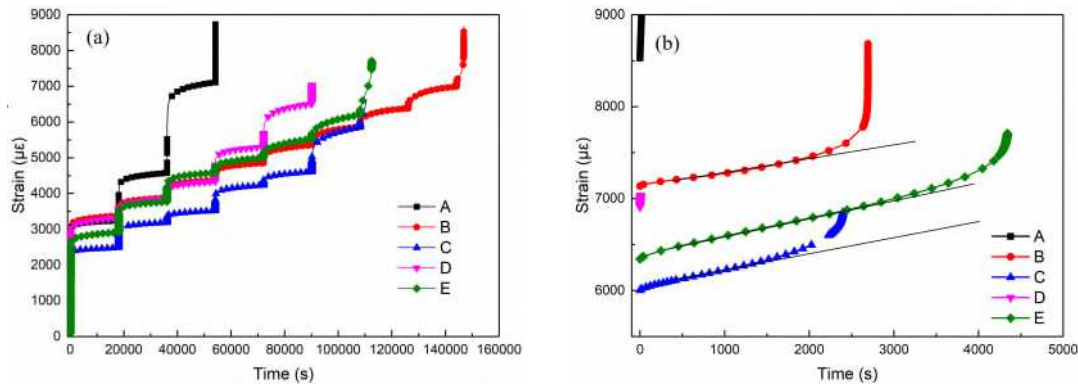
206 The instantaneous strain at the first step was relatively large because of the compaction of
207 the micropores, and then, the instantaneous strain decreased with the increase in the SSR except
208 for the loading steps that changed from a 10% UCS increment to a 20% UCS increment. The
209 instantaneous strain of the last step of the three groups of B, C, and E was only about 146 $\mu\epsilon$,
210 which means that the backfill column hardens during the step-by-step loading process, and the
211 stiffness increases. However, the instantaneous strain of the last step of the groups of A and D
212 with 20% UCS increment was over 390 $\mu\epsilon$ which was larger than twice the instantaneous strain
213 produced by 10% UCS increment, indicating that the step-by-step loading increment has a great
214 influence on the internal damage of the backfill column.

215 As the SSR increased, the creep strain decreased first and then increased. Under the high
216 SSR, the creep strain was greater than the instantaneous strain, indicating the obvious
217 rheological characteristics of the CGBM column. In addition, the difference between the creep
218 strain and the instantaneous strain at each step increased with the increase in the SSR. For some
219 20% UCS increment steps, the creep strain was less than the instantaneous strain. It means that
220 the 20% UCS increment produced more microcracks at the instantaneous loading process,
221 which caused damage to the backfill column.

222 Except for group A which represents that the hydraulic support moves a long distance each
223 time, resulting in a large loading increment at each step, the creep failure strengths of the other
224 4 groups were all larger than the UCS. It means that, under the small increment step-by-step
225 load, the unconfined cemented gangue backfill column will show the axial creep hardening
226 characteristic, which is beneficial for the stability of the backfill column.

227 Fig. 7(b) shows the creep strain–time curves during the creep instability stage. The creep

228 instability of the CGBM samples had three typical creep stages: attenuation creep, stable creep,
 229 and accelerated creep. Before entering the creep accelerated stage, the creep strain rate of the
 230 different loading paths in the stable creep stage was almost the same, for example, the creep
 231 strain rates of samples B, C, and E were ranged from 0.173 $\mu\epsilon/s$ to 0.195 $\mu\epsilon/s$, and the average
 232 strain rate was 0.187 $\mu\epsilon/s$. This creep strain rate could be defined as the critical value of the
 233 creep instability of the backfill column under step-by-step load, that is, once it reaches this creep
 234 rate, the backfill column is considered to enter the creep acceleration stage.



235
 236 **Fig. 7.** (a) Strain–time curve under step-by-step load. (b) Strain–time curve during the creep instability process.

237 **Table 3** The axial strain development under step-by-step load.

| SSR | A / ($\mu\epsilon$) | | B / ($\mu\epsilon$) | | C / ($\mu\epsilon$) | | D / ($\mu\epsilon$) | | E / ($\mu\epsilon$) | |
|-----|-----------------------|--------------|-----------------------|--------------|-----------------------|--------------|-----------------------|--------------|-----------------------|--------------|
| | Instantaneous strain | Creep strain |
| 0.4 | 3418.61 | 667.39 | 2862.79 | 406.51 | 2127.29 | 231.35 | 2804.53 | 443.84 | 2464.07 | 363.44 |
| 0.5 | | | 235.87 | 257.19 | | | 238.74 | 242.84 | | |
| 0.6 | 761.33 | 931.97 | 211.66 | 279.35 | 442.61 | 254.73 | 209.61 | 269.50 | 528.75 | 326.93 |
| 0.7 | | | 189.51 | 296.16 | 169.82 | 162.44 | | | | |
| 0.8 | 517.26 | 2099.40 | 171.05 | 332.67 | | | 460.25 | 498.39 | 416.35 | 392.56 |
| 0.9 | | | 158.75 | 347.85 | 401.99 | 277.71 | | | 158.75 | 265.81 |
| 1.0 | 432.35 | - | 153.41 | 361.39 | 150.13 | 228.48 | 383.54 | 831.89 | 149.31 | 381.08 |
| 1.1 | | | 148.49 | 460.24 | | | | | 143.16 | 523.01 |
| 1.2 | | | 146.85 | - | 337.18 | 911.87 | 396.25 | - | 144.82 | - |
| 1.3 | | | | | 146.44 | - | | | | |

238 3.2.3 Instantaneous deformation modulus

239 The ratio of the axial instantaneous stress increment to the axial instantaneous strain
 240 increment under each loading step was defined as the instantaneous deformation modulus (IDM)
 241 (Fan et al. 2005). Fig. 8 shows the relationship between IDM and SSR. The IDM showed an
 242 upward trend as a whole, but was affected by the loading increment and paths. Group A and

243 Group E were applied with 20% UCS increment before 0.8 UCS, and their IDM growth rate
244 was basically the same, but after over 0.8 UCS, group A still loaded 20% UCS increment and
245 destroyed, while the IDM of group E using the 10% UCS increment increased gradually until
246 1.1 UCS. Group B and D were both applied with 10% UCS increment before 0.6 UCS, and the
247 growth rate of IDM remained the same, but after 0.6 UCS, the group D was applied with a 20%
248 UCS increment and the IDM decreased rapidly; however, the IDM of group B increased
249 continuously with 10% UCS increment. Before 0.7 UCS, the increase of IDM of Group C was
250 consistent with group B and D, and even at 0.7 UCS, the IDM of group C was greater than that
251 of group B and D, but the IDM dropped rapidly when the SSR increased from 0.7 to 0.9, and
252 then when it was loaded with 10% UCS increment, the IDM increased again. The IDM has the
253 following characteristics:

254 $SSR \leq 0.6$, comparing the group B, although the group E was loaded uniformly with a 20%
255 UCS increment when SSR was less than 0.8, the IDM of the two groups was the same in the
256 later period, which means that the IDM of the backfill column does not be affected by the
257 loading increment in the low-stress stage. However, loading in a 10% UCS increment made the
258 backfill column more compact than the 20% UCS increment. $0.6 < SSR \leq 0.8$, the IDM of
259 the backfill column was affected by the loading increment. An increase of 20% UCS, by
260 contrast with a 10% UCS increment, would cause the internal microcracks of the backfill
261 column to continue to grow and damage inside the backfill column. $0.8 < SSR$, the IDM of
262 the backfill column was more sensitive to the step-by-step loading increment, that is, the large
263 increment could cause more damage. For example, the IDM of the backfill column with 20%
264 UCS as the load increment was much lower than that of the 10% UCS. In the low-stress levels,
265 the IDM increased gradually, which showed the creep hardening property and the backfill
266 column hardened; in the medium-stress level, creep hardening and damage competed with each
267 other and continued to develop. In the high-stress level, the IDM had a decreasing trend, which
268 means that the damage in the backfill column accumulated continuously, and the viscosity
269 coefficient decreased.

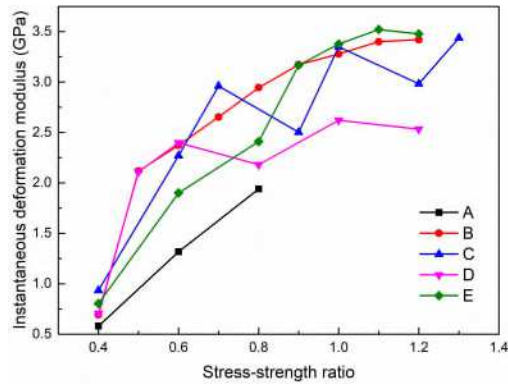


Fig. 8. Development of instantaneous deformation modulus.

The backfill column has the axial creep hardening property. The degree of creep hardening can be expressed by the increment of the IDM under unit stress (MPa), that is, the IDM growth rate $\dot{E}(\sigma)$ (Chen et al. 2016b), calculated as follows:

$$\dot{E}(\sigma) = \frac{E_{\max} - E_{\min}}{\sigma_{E_{\max}} - \sigma_{E_{\min}}} \quad (1)$$

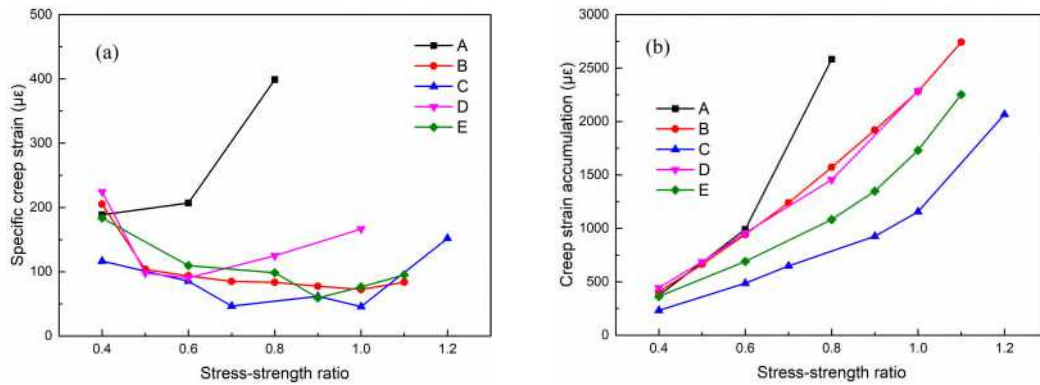
Where E_{\max} is the maximum value of the IDM (MPa) during the step-by-step loading creep process, E_{\min} is the IDM (MPa) at the first stress level, $\sigma_{E_{\max}}$ (MPa) and $\sigma_{E_{\min}}$ (MPa) are the corresponding stress of E_{\max} and E_{\min} , respectively.

The degree of creep hardening of groups B ($0.678 \times 10^5\%$) and E ($0.772 \times 10^5\%$) are much higher than that of groups C ($0.553 \times 10^5\%$) and D ($0.385 \times 10^5\%$), which means that the 20% UCS increment can cause more damage inside of the backfill column after 0.6 UCS. More new microcracks are created in the instantaneous loading process and the original cracks expand obviously. The creep hardening degree of the CPB in the results of Chen et al. (2016b) is $1.2 \times 10^5\%$, which is much larger than the CGBM and proves that the porosity of the CPB is higher. The IDM growth rate in the results of Fan et al. (2005) of red sandstone is $0.593 \times 10^5\%$, which is consistent with the CGBM.

3.2.4 Relationship between creep strain and SSR

Fig. 9(a) shows the creep strain of each SSR under respectively unit stress under step-by-step load. It can be seen that the unit creep strain showed a trend of decrease first and then increase, but the turning point was related to the step-by-step loading paths. Fig. 9(b) shows the accumulation of creep strain. It can be seen that the accumulation of creep strain increased with the increase in SSR, and the growth rate increased gradually. There is an obvious turning point

293 in the curve under various loading paths. Except for group A, the turning points were between
 294 0.9 SSR and 1.0 SSR, which means that there is a stress threshold of the backfill column. When
 295 the stress value was less than the stress threshold, the creep rate would decay gradually; when
 296 the stress value was greater than the stress threshold, the creep rate at the stable stage was almost
 297 constant or even entered the creep failure stage.



298
 299 **Fig. 9.** (a) Specific creep strain at different stress–strength ratios; (b) Accumulation of creep strain.

300 3.3 Lateral deformation under step-by-step load

301 3.3.1 Relationship between lateral strain and SSR

302 Table 4 shows the instantaneous strain and creep strain at axial and lateral (axial
 303 compressive strain is set to a positive value) of group B in the entire step-by-step loading
 304 process. Fig. 10 shows the instantaneous strain and creep strain at axial and lateral of the backfill
 305 column at various SSRs. The lateral deformation has the following characteristics:

306 As the SSR increased, the lateral instantaneous strain decreased first and then increased,
 307 while the axial instantaneous strain decreased continuously. When the SSR exceeded 1.1, the
 308 lateral instantaneous strain increased sharply, showing a large increase in damage. The lateral
 309 instantaneous strain and lateral creep strain at each side of various positions of the backfill
 310 column were different.

311 When SSR was less than 0.6, the lateral creep strain at different places was negative, which
 312 means that the cracks produced during the instantaneous loading step closed gradually during
 313 the creep process. In other words, the lateral position of the backfill column shrunk during the
 314 creeping process. As the SSR increased ($SSR \geq 0.6$), the lateral creep strain increased
 315 continuously, which means that the cracks expanded during the creep process. The creep strain
 316 of the axial was larger than that of the lateral, but in the later step-by-step loading process, the

317 lateral creep strain developed faster than the axial. For example, when the SSR was 0.6, the
 318 axial creep strain and the lateral creep strain (Middle Left) accounted for 1.32% and 3.9% of
 319 the total strain, respectively; and when the SSR was 1.1, the axial creep strain accounted for
 320 4.31%, and lateral creep strain accounted for 5.26%; however, when the SSR reached 1.2, axial
 321 creep strain accounted for 9.59% and lateral creep strain accounted for 23.09%.

322 Fig. 10(a) shows that the instantaneous strain of axial tended to stabilize after the first
 323 loading step; however, the increase of SSR had a great influence on the development of lateral
 324 instantaneous strain after the first loading step. The turning point of lateral instantaneous strain
 325 was around 0.9 SSR, while the turning point of axial instantaneous strain was around 1.0 SSR,
 326 which means that the stress threshold of axial direction was greater than that of the lateral
 327 direction. Fig. 10(b) shows that the turning point of lateral creep strain and axial creep strain
 328 was 0.9 SSR. When the stress value was lower than the stress threshold, the creep strain tended
 329 to a certain value, showing the characteristics of attenuation creep; when the load was higher
 330 than the stress threshold, the creep strain increased with time, showing the characteristics of a
 331 stable creep and even an accelerated creep.

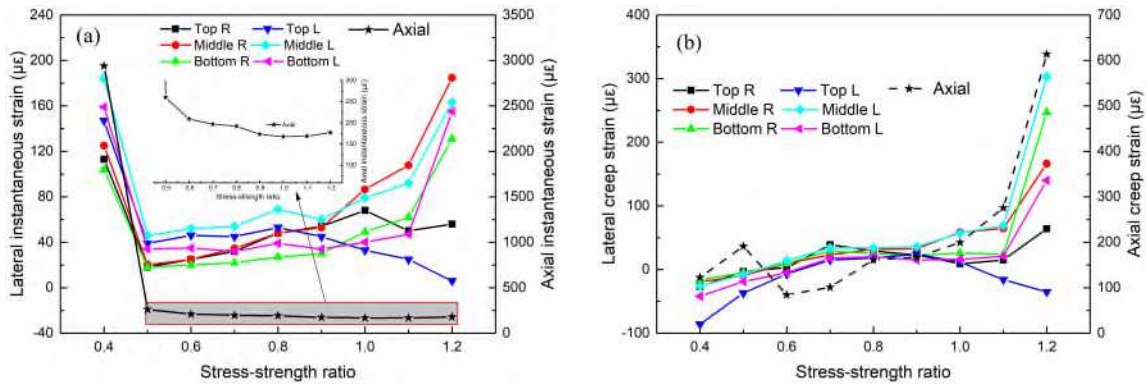
332

333 **Table 4** The axial strain and lateral strain of group B under step-by-step load.

334 Notes: IS and CS represents the instantaneous strain and creep strain, respectively. R and L represent the right side
 335 and left side of the test sample, respectively.

| Position | Axial ($\mu\epsilon$) | | Top R ($\mu\epsilon$) | | Middle R ($\mu\epsilon$) | | Bottom R ($\mu\epsilon$) | | Top L ($\mu\epsilon$) | | Middle L ($\mu\epsilon$) | | Bottom L ($\mu\epsilon$) | |
|----------|-------------------------|--------|-------------------------|-----|----------------------------|--------|----------------------------|-----|-------------------------|-----|----------------------------|-----|----------------------------|-----|
| | IS | CS | IS | CS | IS | CS | IS | CS | IS | CS | IS | CS | IS | CS |
| 0.4 | 2939.49 | 122.65 | 113 | -27 | 125 | -19.23 | 104 | -16 | 147 | -86 | 184 | -26 | 159 | -42 |
| 0.5 | 260.06 | 191.15 | 18 | -3 | 20.19 | -9.62 | 18 | -5 | 39 | -37 | 46 | -8 | 34 | -19 |
| 0.6 | 209.20 | 84.50 | 25 | 3 | 25 | 9.62 | 20 | 10 | 46 | -7 | 52 | 14 | 35 | -5 |
| 0.7 | 196.89 | 100.90 | 32 | 39 | 34.61 | 23.08 | 22 | 29 | 45 | 15 | 54 | 34 | 32 | 18 |
| 0.8 | 192.38 | 161.61 | 48 | 29 | 48.08 | 31.73 | 27 | 25 | 53 | 18 | 69 | 34 | 39 | 20 |
| 0.9 | 173.10 | 166.95 | 54 | 23 | 52.88 | 32.7 | 30 | 22 | 45 | 24 | 60 | 36 | 34 | 15 |
| 1.0 | 167.36 | 199.35 | 68 | 9 | 86.53 | 58.66 | 49 | 26 | 33 | 12 | 79 | 57 | 40 | 16 |
| 1.1 | 168.59 | 275.65 | 50 | 15 | 107.69 | 64.42 | 62 | 24 | 25 | -16 | 92 | 69 | 47 | 21 |
| 1.2 | 173.21 | 613.65 | 56 | 64 | 184.62 | 166.34 | 131 | 247 | 6 | -35 | 163 | 303 | 155 | 140 |

336



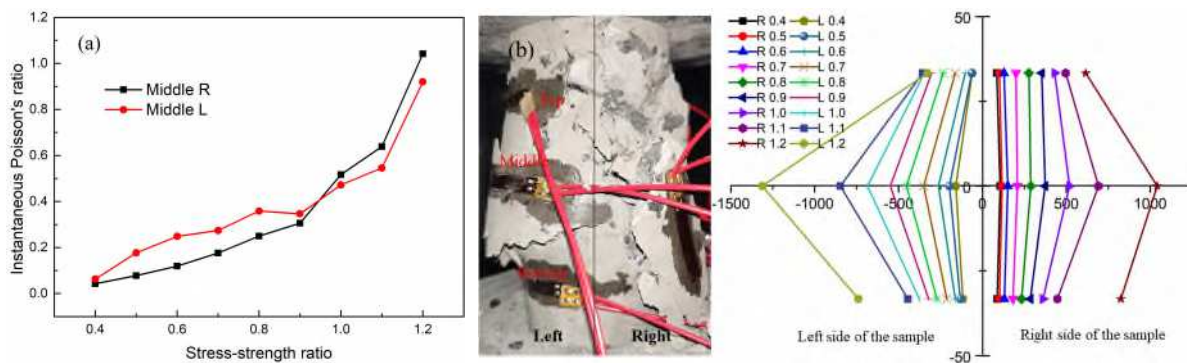
337
338 **Fig. 10.** Development of (a) instantaneous strain and (b) creep strain of group B under step-by-step load.

339 **3.3.2 Instantaneous Poisson's ratio and accumulation of lateral strain**

340 The ratio of the lateral strain to the axial strain under the unit stress increment was defined
 341 as the instantaneous Poisson's ratio (Fan et al. 2005). The instantaneous Poisson's ratio of the
 342 backfill column was calculated by using the lateral instantaneous strain in the middle of the left
 343 and right positions. Fig. 11(a) shows the relationship between the instantaneous Poisson's ratio
 344 and the SSR. It can be seen that the instantaneous Poisson's ratio of the backfill showed a
 345 concave upward trend with the increase in SSR, and it was much greater than the value of the
 346 Poisson's ratio in the conventional test (Sun et al. 2019). There is a turning point at 0.9 SSR,
 347 and the instantaneous Poisson's ratio increased sharply after 0.9 SSR. During the step-by-step
 348 loading process, the axial instantaneous strain decreased with the increase in SSR; however,
 349 after the first loading step, the lateral instantaneous strain increased with the increase in SSR.
 350 It means that the cemented gangue backfill column showed axial creep hardening property and
 351 lateral creep softening property as a whole during the step-by-step loading process. With the
 352 increase of creep time and SSR, the microcracks expanded during the creep process and the
 353 damage accumulated at the same time, and the plastic deformation of the lateral was higher
 354 than that of the axial, which shows the obvious expansion phenomenon.

355 Fig. 11(b) shows the accumulation of lateral strain on the left and right side of group B
 356 under the step-by-step load. The lateral deformation at the middle positions on the left side and
 357 right side of specimen B increased gradually with the increase in SSR and was greater than the
 358 deformation at the other positions on the same side. Besides, with the increase of SSR, the
 359 lateral expanding rate increased significantly. When the lateral localized deformation reached
 360 the limit, the corresponding position was damaged, producing macrocracks on the surface and

361 the specimen lost its bearing capacity instantly (Sun et al. 2019). In the actual engineering, the
 362 top and bottom of the backfill column had a hoop effect due to the friction of the roof; therefore,
 363 it had a certain protective effect on the ends of the backfill column (Du et al. 2019a). However,
 364 in the middle of the unconfined backfill column was subjected to tensile stress, it was easy to
 365 produce macrocracks, which led to sudden instability of the backfill column. Thus, it is
 366 necessary to set the around constraint in the middle part of the backfill column to restrict the
 367 lateral deformation, such as the use of stirrups. The expansion of the backfill column because
 368 of the production of cracks makes the stirrups tensile, and then the stirrups restrict conversely
 369 the continuous expansion of the backfill column, increasing the stability of the backfill column
 370 (Du et al. 2019b).



371
 372 **Fig. 11.** (a) Curve of instantaneous Poisson's ratio; (b) Accumulation of the lateral strain of sample B.

373 3.4 Instability of the backfill column

374 3.4.1 Development of cracks under step-by-step load

375 With the increase of SSR, the lateral of the backfill column expanded outwards
 376 continuously. The non-uniform lateral deformation led to excessive localized deformation at a
 377 certain position of the backfill column, which mainly occurred in the middle places. The tensile
 378 stress on the surface exceeded the limit of CGBM and caused macrocracks, which led to the
 379 reduction of the actual bearing area, and the increase of the actual stress. Therefore, the damage
 380 of the backfill column intensified suddenly, and the backfill column underwent creep failure.
 381 The evolution of damage of the backfill column under step-by-step load associates with the
 382 development of cracks, which could be divided into 4 stages according to the above analyses,
 383 as shown in Fig. 12. In compression, the orientation of microcracks is preferred to be parallel
 384 to the loading direction (Rossi et al. 2012). The density of microcracks generated during the

385 creep process depends on the propagation of the microcracks created during the instantaneous
386 loading process (initial microcracks), but also on the creation of new microcracks.

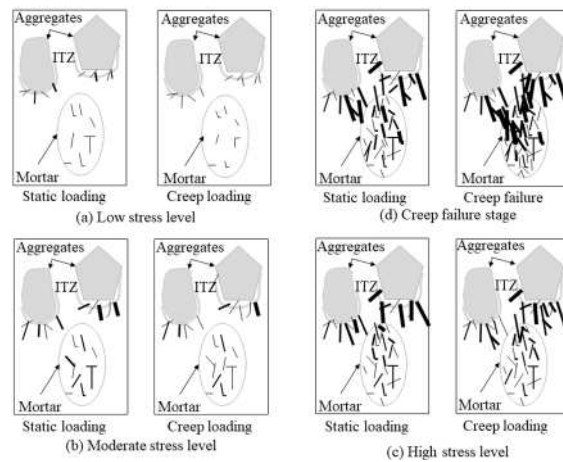
387 When SSR is less than 0.6 (Fig. 12(a)). The backfill column is in the elastic stage. After
388 the initial instantaneous loading step, microcracks are produced in the interfacial transition zone
389 (ITZ) (Al-Mufti et al. 2016), and a small number of microcracks are generated in the mortar.
390 However, during the constant load stage, most microcracks in the mortar can close, and partial
391 microcracks in the ITZ can close at the same time; thus, the entire backfill column is stable.

392 When SSR is 0.6 – 0.9 (Fig. 12(b)). The backfill column enters the plastic stage. After the
393 static loading steps, new cracks can be generated in the ITZ and the mortar, and the existing
394 cracks can expand. There is a competition between the creation of new microcracks during the
395 sustained load and the closure of the previous microcracks created during the instantaneous
396 loading. In the creep stage, some microcracks can close, a small part of the microcracks can
397 expand, if there is no external dynamic disturbance (Sun et al. 2018), the backfill column
398 stabilizes gradually during the creep process.

399 When SSR is greater than 0.9 (Fig. 12(c)). After the instantaneous loading step, more new
400 cracks are produced in the ITZ and mortar of the backfill column, and the existing cracks can
401 expand. The density of microcracks increases significantly. During the creep process, more
402 cracks can expand and a few cracks can close. As active microcracks (opened) that were created
403 during the sustained loading are more numerous than the closed ones, localization of the new
404 microcracks can occur at the macrocrack front tip, hence leading to macrocrack propagation
405 (Rossi et al. 2012). Consequently, the cracks in mortar and ITZ tend to connect to form larger
406 macrocracks, but it will take a long time for creep instability to occur and depends on the stress
407 level.

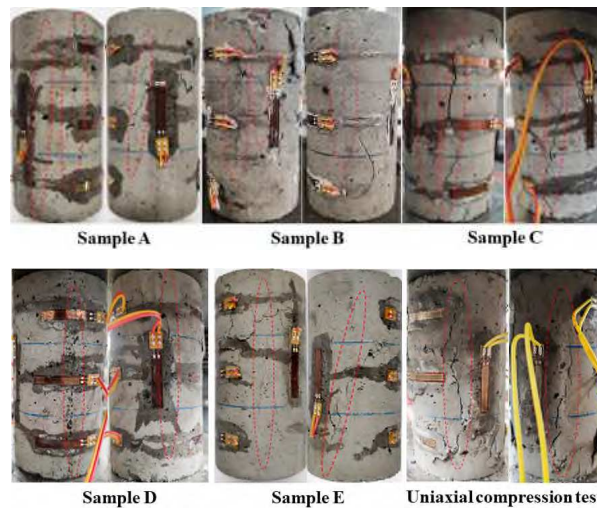
408 If the stress increases on this basis, as shown in Fig. 12(d), the backfill column will enter
409 the creep failure stage rapidly. During the instantaneous loading process, a large number of new
410 cracks can be created in the ITZ and the mortar, and the existing cracks can extend significantly
411 during the creep process. The elastic strain energy accumulated during the instantaneous
412 loading process is larger than the energy that the expansion of cracks needs. When the cracks

413 in the ITZ and the cracks in the mortar are connected, meantime, tension cracks appear on the
 414 surface of the backfill column, and macrocracks form inside the backfill column, the
 415 macrocracks penetrate each other. As shown in Fig. 13, there are many obvious tensile cracks
 416 on the surface of the sample because of the Poisson's effect, accompanied by shear and peeling
 417 failure. Compared to the uniaxial compression test, the creep failure under step by step was
 418 more quickly and intensely. There's no residual bearing stage of the creep failure, and the
 419 backfill column loses the bearing capacity immediately (Ran et al. 2021).



420
421

Fig. 12. Schematic description of the production of cracks and cracking processes.



422

423
424

Fig. 13. Failure forms of the CGBM samples.

425 **3.4.2 Effects of step-by-step loading increment and paths on the cracking**

426 The bearing capacity of the backfill column was affected by the increment during the step-
 427 by-step loading process. The main reason is that the 20% UCS increment will affect the
 428 generation and expansion of cracks in the backfill column, that is, under the condition of large

429 increment, the internal cracks of the backfill column will develop more fully during the static
430 loading process. When entering the creeping stage, the localized stress concentration caused at
431 the static loading process will redistribute and homogenize, forming a state of coexistence of
432 crack closure and crack development.

433 The effect of loading increment on the cracking also depends on the stress level. Under
434 low-stress levels, microcracks are created in the backfill column at the static loading, because
435 the length of the crack is relatively short, most of the microcracks can close during the creep
436 process; thus, the loading increment will not affect its internal crack system. Under medium
437 and high-stress levels, for the uniform step-by-step load, the 20% UCS loading increment can
438 cause more microcracks in the backfill column during the static loading process, and cracks can
439 expand more fully during the loading process. Consequently, compared with the 10% UCS
440 loading increment, greater irreversible damage is produced in the backfill column. Although
441 some microcracks can close during the creep process, more microcracks expand gradually and
442 connect under constant pressure. For the alternate loading path, the 20% UCS increment still
443 causes more obvious damage, but when the next level of 10% UCS increment is applied, the
444 damage will not increase rapidly. Consequently, the crack system inside the backfill column is
445 more stable compared with the 20% UCS increment uniform load.

446 Therefore, the step-by-step loading test can be used to study the failure process of the
447 backfill column during the advancement of the coal mining face. In addition, the failure process
448 of the backfill column can be influenced by the step-by-step loading paths. In order to avoid the
449 instability of the goaf, the design of moving distance and cycle of the hydraulic support should
450 match the bearing capacity of the backfill column.

451 **4 Constitutive model of the creep strain under step-by-step load**

452 **4.1 Establishment of the model**

453 Through the combination of the various rheological elements, which can characterize the
454 basic properties of materials, such as elasticity, viscoelasticity, viscosity or damage, a
455 comprehensive performance of materials could be depicted (Han et al. 2017). The strain
456 development at each step of the CGBM column under step-by-step load can be divided into

457 three stages, instantaneous strain, recoverable viscoelastic strain, and the uncoverable viscous
 458 strain caused by the generation of microcracks under high-stress levels. Therefore, a creep
 459 model for the backfill column under step-by-step load can be established by assembling the
 460 following rheological components. As shown in Fig. 14, the constitutive model is connected by
 461 the Maxwell model, Kelvin model, and the Bingham model.

462 As stated, the backfill column would be damaged under a relatively high-stress level and
 463 its creep strain presents nonlinearly. In the model, the Bingham model was used to feature the
 464 nonlinear aspect of the creep. If the stress exceeds σ_{VP} of the Saint-Venant body, which
 465 signifies damage, Bingham model takes its effect, or else its strain is zero. The instantaneous
 466 deformation modulus of the backfill column under step-by-step load increased gradually; thus,
 467 the value of the Maxwell model's spring body was determined by the IDM. According to the
 468 experimental data, as shown in Fig. 8, groups B and E are set as examples, the IDM of the
 469 backfill column under step-by-step load was fitted.

$$470 \quad E_1 = -2.67 + 11.39 \times SSR - 5.34 \times SSR^2 \quad (R^2 = 0.951 \text{ group B}) \quad (2)$$

$$471 \quad E_1 = -0.00137 - 0.0137 \times SSR + 0.224 \times SSR^2 - 0.126 \times SSR^3 \quad (R^2 = 0.965 \text{ group E}) \quad (3)$$

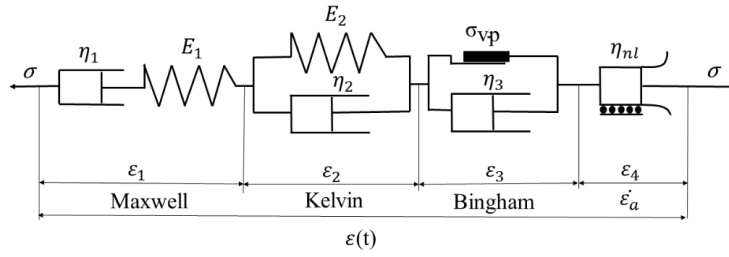
472 Where E_1 is the elastic modulus of the Maxwell model, and SSR is the stress–strength ratio.

473 As shown in Fig. 7(b), the creep strain rate is almost a constant before entering the
 474 accelerated creep stage, which means that this creep strain rate could be regarded as the trigger
 475 of the creep model whether to start the accelerated stage. To describe the accelerated creep
 476 strain at the failure stage, a nonlinear dashpot with a creep strain rate trigger was connected to
 477 the viscoelastic-plastic model to construct the creep model, as shown in Fig. 14. The creep strain
 478 rate-triggered nonlinear dashpot has a rigid body when the creep strain rate is less than $\dot{\varepsilon}_a$ and
 479 does not work. When the creep strain rate is greater than $\dot{\varepsilon}_a$, the nonlinear dashpot is triggered;
 480 its constitutive relation is given by (4) (Qi et al. 2012).

$$481 \quad \begin{cases} \sigma = \eta_{nl} \dot{\varepsilon}_{nl} & (\dot{\varepsilon} > \dot{\varepsilon}_a) \\ \varepsilon_{nl} = 0 & (\dot{\varepsilon} \leq \dot{\varepsilon}_a) \end{cases} \quad (4)$$

482 Where η_{nl} is the viscosity coefficient of the nonlinear dashpot, $\dot{\varepsilon}$ is the creep strain rate, $\dot{\varepsilon}_a$

483 is the trigger value of the nonlinear dashpot.



484
485

Fig. 14. Modified viscoelastic-plastic model for the creep of CGBM.

486 The axial strain of the CGBM column at each step could be obtained by

$$487 \quad \varepsilon_n(t) = \begin{cases} \frac{\sigma}{E_{1n}} + \frac{\sigma}{\eta_{1n}} t + \frac{\sigma}{E_{2n}} (1 - e^{-\frac{E_{2n} t}{\eta_{2n}}}) & (\sigma < \sigma_{VP}, \quad \varepsilon^g < \varepsilon_a^g) \\ \frac{\sigma}{E_{1n}} + \frac{\sigma}{\eta_{1n}} t + \frac{\sigma}{E_{2n}} (1 - e^{-\frac{E_{2n} t}{\eta_{2n}}}) + \frac{\sigma - \sigma_{VP}}{\eta_{3n}} t & (\sigma \geq \sigma_{VP}, \quad \varepsilon^g \leq \varepsilon_a^g) \\ \frac{\sigma}{E_{1n}} + \frac{\sigma}{\eta_{1n}} t + \frac{\sigma}{E_{2n}} (1 - e^{-\frac{E_{2n} t}{\eta_{2n}}}) + \frac{\sigma - \sigma_{VP}}{\eta_{3n}} t + \frac{\sigma}{2\eta_{nl}} \tau^2 & (\sigma \geq \sigma_{VP}, \quad \varepsilon^g > \varepsilon_a^g) \end{cases} \quad (5)$$

488 Where $\varepsilon_n(t)$ is the strain at each step, and n represents the step number; σ is the stress
489 loading on the test sample; t means the creep loading time at each step; E_{1n} and E_{2n} are
490 the elastic parameters of the spring element; η_{1n} , η_{2n} and η_{3n} are the viscosity coefficients
491 of the Newton dashpot; σ_{VP} is critical stress to trigger the Saint Venant body, and it is
492 activated when the SSR is over the 0.6; $\tau = t - t \Big|_{\varepsilon^g > \varepsilon_a^g}$ and $t \Big|_{\varepsilon^g > \varepsilon_a^g}$ is the time for the start
493 of accelerated creep stage.

494 To describe the complete axial deformation process of backfill column under step-by-step
495 load, the total strain was accumulated and can be expressed as

$$496 \quad \varepsilon_{total} = \sum_1^n \varepsilon_n(t) \quad (6)$$

497 Where ε_{total} is the total axial strain; n represents the step number.

498 **4.2 Determination of the parameters for the constitutive model**

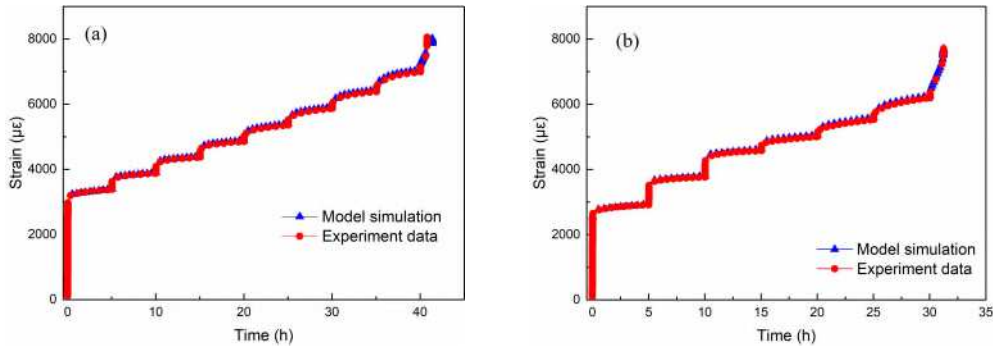
499 The parameters of samples B and E in the viscoelastic-plastic model were fitted, and the
500 fitting results are shown in Table 5. The calculated results and measured data were compared,
501 as shown in Fig. 15. The results of the two groups were highly consistent. It shows that the
502 nonlinear creep model established in this paper is reasonable and reliable. Thus, the nonlinear
503 creep constitutive model can accurately depict the axial strain development of the backfill

504 column under step-by-step load.

505 **Table 5** Parameter fitting results of samples B and E.

| Sample | Stress(MPa) | SSR | E_1 (Gpa) | η_1 (MPa · h) | E_2 (Mpa) | η_2 (MPa · h) | η_3 (MPa · h) | η_{nl} (MPa · h ²) | R-square |
|--------|-------------|-----|-------------|--------------------|-------------|--------------------|--------------------|-------------------------------------|----------|
| B | 2.02 | 0.4 | 0.69 | 58524.092 | 8216.675 | 844.839 | - | - | 0.9994 |
| | 2.52 | 0.5 | 2.11 | 101656.551 | 17838.637 | 4376.277 | - | - | 0.9729 |
| | 3.02 | 0.6 | 2.37 | 125538.527 | 18080.891 | 4805.288 | - | - | 0.9858 |
| | 3.52 | 0.7 | 2.65 | 130629.873 | 20939.243 | 6700.095 | -9.63e22 | - | 0.9910 |
| | 4.025 | 0.8 | 2.94 | 112494.902 | 25147.119 | 10460.961 | -5.27e26 | - | 0.9952 |
| | 4.528 | 0.9 | 3.17 | 133037.883 | 24546.043 | 14754.544 | 4.46e20 | - | 0.9972 |
| | 5.03 | 1.0 | 3.28 | 156570.82 | 24025.577 | 15825.899 | 1.57e27 | - | 0.9968 |
| | 5.53 | 1.1 | 3.4 | 151209.82 | 19520.561 | 16785.725 | 1.15e22 | - | 0.9984 |
| | 6.04 | 1.2 | 3.42 | 10351.7587 | 1.64e24 | 2.26e5 | -3.13e19 | 39.726 | 0.9878 |
| E | 2.013 | 0.4 | 0.777 | 59632.399 | 9431.944 | 1364.912 | - | - | 0.9645 |
| | 3.019 | 0.6 | 1.899 | 110674.062 | 14921.977 | 1736.174 | - | - | 0.9628 |
| | 4.024 | 0.8 | 2.409 | 127934.897 | 16063.746 | 2721.757 | 3.46e27 | - | 0.9665 |
| | 4.526 | 0.9 | 3.166 | 144153.869 | 46665.205 | 20798.086 | 3.64e5 | - | 0.9966 |
| | 5.029 | 1.0 | 3.376 | 101077.646 | 36418.481 | 17430.376 | 4.44e27 | - | 0.9968 |
| | 5.532 | 1.1 | 3.521 | 92944.718 | 23485.735 | 14750.221 | 4.77e21 | - | 0.9975 |
| | 6.034 | 1.2 | 3.476 | 7524.703 | -7.21e12 | 4.40e11 | 1.01e20 | 28326.812 | 0.9201 |

506



507 **Fig. 15.** Comparison of the experimental and simulation results of samples (a) B and (b) E.

508

509 **5 Conclusions**

510 In this study, five step-by-step loading paths are used to simulate the loading history of the
 511 roof loading to the backfill columns. The deformation and instability properties of the CGBM
 512 column under step-by-step load were analyzed, and the following conclusions were drawn:

- 513 (1) As SSR increases, the axial instantaneous strain decreases gradually, the axial creep
 514 strain decreases first and then increases. In the high SSR, the axial creep strain is greater than
 515 the axial instantaneous strain, and the difference between the creep strain and the instantaneous
 516 strain at each step increases with the increase in SSR. The lateral instantaneous strain decreases
 517 first and then increases, while the lateral creep strain increases continuously. When SSR is less

518 than 0.6, the lateral positions of the backfill column shrink during the creeping process. In the
519 high-stress levels, lateral creep strain develops faster than axial creep strain, and the stress
520 threshold of axial is larger than that of lateral.

521 (2) The backfill column shows the axial creep hardening and lateral creep softening
522 properties during the step-by-step loading process. The ultimate stress and its corresponding
523 strain of the backfill column under step-by-step load are greater than those of the uniaxial
524 compression test. The instantaneous deformation modulus shows an upward trend on the whole,
525 but it is affected by the step-by-step loading increment and paths. The instantaneous Poisson's
526 ratio exhibits a concave upward trend and is larger than that in the conventional test.

527 (3) The ultimate bearing capacity of the backfill column under step-by-step loading is
528 related to the step-by-step loading increment and paths, small increment uniform loading \geq large
529 to small increment uniform loading \geq small to large increment uniform loading $>$ large
530 increment uniform loading \geq uniaxial compression. The development of cracks of the backfill
531 column under step-by-step load could be divided into 4 stages according to the SSR. The non-
532 uniformity of the lateral deformation of the backfill column leads to the excessive localized
533 deformation that mostly occurs at the middle of the backfill column and produces macroscopic
534 cracks, which causes the overall instability.

535 (4) The CGBM column has obvious rheological characteristics, and the creep strain of the
536 backfill column has nonlinear characteristics. Under different step-by-step loading paths, the
537 axial creep strain rate is nearly a constant before entering the accelerated creep stage. A non-
538 linear creep constitutive model with a creep strain rate trigger was established to express the
539 development of the axial strain of the backfill column under the step-by-step load.

540 In this research, the small size sample was tested, in the future, the large size sample will
541 be tested, and the damage will be monitored using acoustic emission and ultrasonic equipment
542 during the step-by-step loading process.

543 **Availability of data and materials**

544 The datasets used and/or analyzed during the current study are available from the
545 corresponding author on reasonable request.

546 **Author contribution**

547 Yuxia Guo: conceptualization, funding acquisition, methodology, and writing-review and
548 editing. Hongyu Ran: Experiment, investigation and writing-original draft. Guorui Feng:
549 investigation, supervision, funding acquisition, and writing-review and editing. Xianjie Du:
550 writing-review and editing. Yonghui Zhao: experiment and investigation. Wenshuo Xie:
551 experiment and investigation.

552 **Funding**

553 This work is supported by the National Natural Science Foundation of China (51974192),
554 Shanxi province postgraduate education innovation project (2020SY567), Distinguished Youth
555 Funds of National Natural Science Foundation of China (51925402), Shanxi Science and
556 Technology Major Project (20201102004), and the Applied Basic Research Project of Shanxi
557 Province (201801D121092).

558 **Declarations**

559 **Ethics approval** Not applicable

560 **Consent to participate** Not applicable

561 **Consent for publication** Not applicable

562 **Competing interest** The authors declare no competing interests

563 **References**

- 564 Al-Mufti R L, Fried A N (2016) Pulse velocity assessment of early age creep of concrete. *Constr Build*
565 *Mater* 121:622-628. <https://doi.org/10.1016/j.conbuildmat.2016.06.015>
- 566 Cao S, Song WD (2017) Effect of filling interval time on the mechanical strength and ultrasonic
567 properties of cemented coarse tailing backfill. *Int J Miner Process* 166:62-68.
568 <https://doi.org/10.1016/j.minpro.2017.07.005>
- 569 Cao S, Yilmaz E, Song WD, Yilmaz E, Xue GL (2019) Loading rate effect on uniaxial compressive
570 strength behavior and acoustic emission properties of cemented tailings backfill. *Constr Build*
571 *Mater* 213:313-324. <https://doi.org/10.1016/j.conbuildmat.2019.04.082>
- 572 Chen SJ, Yin DW, Cao FW, Liu Y, Ren KQ (2016a) An overview of integrated surface subsidence-
573 reducing technology in mining areas of China. *Nat Hazards* 81(2):1129-1145.
574 <https://doi.org/10.1007/s11069-015-2123-x>
- 575 Chen SJ, Liu XY, Han Y, Guo YH, Ren KQ (2016b) Experimental study of creep hardening
576 characteristic and mechanism of filling paste. *Chin J Rock Mech Eng* 35(03):570-578.
577 <https://doi.org/10.13722/j.cnki.jrme.2015.1228> (in Chinese)
- 578 Chen SJ, Du ZW, Zhang Z, Yin DW, Feng F, Ma J (2020) Effects of red mud additions on gangue-
579 cemented paste backfill properties. *Powder Technol* 2020: 367.

580 <https://doi.org/10.1016/j.powtec.2020.03.055>

581 Du XJ, Feng GR, Guo YX, Qi TY, Zhang YJ, Guo J (2018) Failure analyses of unconfined CCWBM
582 body in uniaxial compression based on central pressure variation. *Waste Manage Res* 36(2):159-
583 168. <https://doi.org/10.1177/0734242X17748365>

584 Du XJ, Feng GR, Qi TY, Guo YX, Zhang YJ, Wang ZH (2019a) Failure characteristics of large
585 unconfined cemented gangue backfill structure in partial backfill mining. *Constr Build Mater*
586 194:257-265. <https://doi.org/10.1016/j.conbuildmat.2018.11.038>

587 Du XJ, Feng GR, Zhang YJ, Wang ZH, Guo YX, Qi TY (2019b) Bearing mechanism and stability
588 monitoring of cemented gangue-fly ash backfill column with stirrups in partial backfill engineering.
589 *Eng Struct* 188:603-612. <https://doi.org/10.1016/j.engstruct.2019.03.061>

590 Fall M, Belem T, Samb S, Benzaazoua M (2007) Experimental characterization of the stress-strain
591 behaviour of cemented paste backfill in compression. *J Mater Sci* 42(11):3914-3922.
592 <https://doi.org/10.1007/s10853-006-0403-2>

593 Fall M, Célestin JC, Pokharel M, Touré M (2010) A contribution to understanding the effects of curing
594 temperature on the mechanical properties of mine cemented tailings backfill. *Eng Geol* 114(3):397-
595 413. <https://doi.org/10.1016/j.enggeo.2010.05.016>

596 Fall M, Pokharel M (2010) Coupled effects of sulphate and temperature on the strength development of
597 cemented tailings backfills: Portland cement-paste backfill. *Cement Concrete Comp* 32(10):819-
598 828. <https://doi.org/10.1016/j.cemconcomp.2010.08.002>

599 Fan QZ, Gao YF (2005) Experimental study on creep properties of rocks under stepwise loading.
600 *Chinese Journal of Geotechnical Engineering* (11):38-41. <https://doi.org/10.3321/j.issn:1000-4548.2005.11.008> (in Chinese)

602 Feng GR, Du XJ, Guo YX, Qi TY, Kang LX (2019) Basic theory of constructional backfill mining and
603 the underground space utilization concept. *J China Coal Soc* 44(1):74-84.
604 <https://doi.org/10.13225/j.cnki.jccs.2018.1598> (in Chinese)

605 Fu ZL, Gao YF, Ning W, Xu JP (2007) Creep of Anisotropic Oil Shale. *J Min Safe Eng* (3):105-108.
606 <https://doi.org/10.3969/j.issn.1673-3363.2007.03.022> (in Chinese)

607 Guo YX, Ran HY, Feng GR, Du XJ, Qi TY, Wang ZH (2020) Effects of curing under step-by-step load
608 on mechanical and deformation properties of cemented gangue backfill column. *J Cent South Univ*
609 27: 3417-3435 <https://doi.org/10.1007/s11771-020-4556-y>

610 Han B, Xie HB, Zhu L, Jiang P (2017) Nonlinear model for early age creep of concrete under
611 compression strains. *Constr Build Mater* 147:203-211.
612 <https://doi.org/10.1016/j.conbuildmat.2017.04.119>

613 Hou C, Zhu WC, Yan BX, Guan K, Niu LL (2019) Analytical and Experimental Study of Cemented
614 Backfill and Pillar Interactions. *Int J Geomech* 19(8). [https://doi.org/10.1061/\(ASCE\)GM.1943-5622.0001441](https://doi.org/10.1061/(ASCE)GM.1943-5622.0001441)

616 Hou J, Guo ZP, Li J, Zhao LJ (2020) Study on triaxial creep test and theoretical model of cemented
617 gangue-fly ash backfill under seepage stress coupling. *Constr Build Mater* 2020:121722.
618 <https://doi.org/10.1016/j.conbuildmat.2020.121722>

619 Jia CJ, Xu WY, Wang RB, Wang SS, Lin ZN (2018) Experimental investigation on shear creep properties
620 of undisturbed rock discontinuity in Baihetan Hydropower Station. *Int J Rock Mech Min* 104:27-
621 33. <https://doi.org/10.1016/j.ijrmms.2018.02.011>

622 Li BL, Lan JQ, Si GY, Lin GP, Hu LQ (2020) NMR-based damage characterisation of backfill material

623 in host rock under dynamic loading. *Int J Min Sci Techno* 30:329-335
624 <https://doi.org/10.1016/j.ijmst.2020.03.015>

625 Li CJ, Xu Y, Feng MM, Pan B (2020) Deformation law and failure mechanism of coal-rock-like
626 combined body under uniaxial loading. *J China Coal Soc* 45(5):1773-1782.
627 <https://doi.org/10.13225/j.cnki.jccs.2019.0625> (in Chinese)

628 Liu JG, Li XT, He T (2020) Application status and prospect of backfill mining in Chinese coal mines. *J*
629 *China Coal Soc* 45(1):141-150. <https://doi.org/10.13225/j.cnki.jccs.YG19.1063> (in Chinese)

630 Liu L, Zhu C, Qi CC, Wang M, Huan C, Zhang B, Song KI-IL (2019) Effects of curing time and ice-to-
631 water ratio on performance of cemented paste backfill containing ice slag. *Constr Build Mater*
632 228:116639. <https://doi.org/10.1016/j.conbuildmat.2019.08.020>

633 Qi CC, Fourie A (2019) Numerical Investigation of the Stress Distribution in Backfilled Stopes
634 Considering Creep Behaviour of Rock Mass. *Rock Mech Rock Eng* 52(9):3353-3371.
635 <https://doi.org/10.1007/s00603-019-01781-0>

636 Qi TY, Feng GR, Li YR, Guo YX, Zhang YJ (2015) Effects of Fine Gangue on Strength, Resistivity,
637 and Microscopic Properties of Cemented Coal Gangue Backfill for Coal Mining. *Shock Vib.*
638 2015:1-11. <https://doi.org/10.1155/2015/752678>

639 Qi YJ, Jiang QH, Wang ZJ, Zhou CB (2012) 3D creep constitutive equation of modified Nishihara model
640 and its parameters identification. *Chin J Rock Mech Eng* 31(2):347-355.
641 <https://doi.org/10.3969/j.issn.1000-6915.2012.02.014> (in Chinese)

642 Ran HY, Guo YX, Feng GR, Qi TY, Du XJ (2021) Creep properties and resistivity-ultrasonic-AE
643 responses of cemented gangue backfill column under high-stress area. *Int J Min Sci Techno* 2021
644 <https://doi.org/10.1016/j.ijmst.2021.01.008>

645 Rossi P, Tailhan J-L, Maou F Le, Gaillet L, Martin E (2012) Basic creep behavior of concretes
646 investigation of the physical mechanisms by using acoustic emission. *Cement Concrete Res*
647 42(1):61-73. <https://doi.org/10.1016/j.cemconres.2011.07.011>

648 Shi GC, Yang XJ, Yu HC, Zhu C (2019) Acoustic emission characteristics of creep fracture evolution in
649 double-fracture fine sandstone under uniaxial compression. *Eng Fract Mech* 210:13-28.
650 <https://doi.org/10.1016/j.engfracmech.2018.09.004>

651 Sun Q, Li B, Tian S, Cai C, Xia YJ (2018) Creep properties of geopolymer cemented coal gangue-fly
652 ash backfill under dynamic disturbance. *Constr Build Mater* 191:644-654.
653 <https://doi.org/10.1016/j.conbuildmat.2018.10.055>

654 Sun Q, Cai C, Zhang SK, Tian S, Li B, Xia YJ, Sun QW (2019a) Study of localized deformation in
655 geopolymer cemented coal gangue-fly ash backfill based on the digital speckle correlation method.
656 *Constr Build Mater* 215:321-331. <https://doi.org/10.1016/j.conbuildmat.2019.04.208>

657 Sun Q, Tian S, Sun QW, Li B, Cai C, Xia YJ, Wei X, Mu QW (2019b) Preparation and microstructure
658 of fly ash geopolymer paste backfill material. *J Cleaner Prod* 225:376-390.
659 <https://doi.org/10.1016/j.jclepro.2019.03.310>

660 Wang F, Jiang BY, Chen SJ, Ren MZ (2019a) Surface collapse control under thick unconsolidated layers
661 by backfilling strip mining in coal mines. *Int J Rock Mech Min* 113:268-277.
662 <https://doi.org/10.1016/j.ijrmms.2018.11.006>

663 Wang J, Song WD, Cao S, Tan YY (2019b) Mechanical properties and failure modes of stratified backfill
664 under triaxial cyclic loading and unloading. *Int J Min Sci Techno* 29:809-814.
665 <https://doi.org/10.1016/j.ijmst.2018.04.001>

-
- 666 Wang HC, Qi TY, Feng GR, Wen XZ, Wang ZH, Shi XD, Du XJ (2021) Effect of partial substitution of corn
667 straw fly ash for fly ash as supplementary cementitious mater. *Constr Build Mater* 280: 122553
668 <https://doi.org/10.1016/j.conbuildmat.2021.122553>
- 669 Wang ZH, Feng GR, Qi TY, Guo YX, Du XJ (2020) Evaluation of static segregation of cemented
670 gangue-fly ash backfill material using electrical resistivity method. *Measurement* 154:107483.
671 <https://doi.org/10.1016/j.measurement.2020.107483>
- 672 Wu CZ, Chen QS, Basack S, Shivakumar K (2018) Laboratory investigation on rheological properties
673 of greenschist considering anisotropy under multi-stage compressive creep condition. *J Struct Geol*
674 114:111-120. <https://doi.org/10.1016/j.jsg.2018.06.011>
- 675 Wu JY, Y Q, Gao Y, Meng B, Jing HW (2021a) Particle size distribution of aggregates effects on
676 mesoscopic structural evolution of cemented waste rock backfill. *Environ Sci Pollut R* 2021
677 <https://doi.org/10.1007/s11356-020-11779-9>
- 678 Wu JY, Jing HW, Meng QB, Yin Q, Yu LY (2021b) Assessment of cemented waste rock backfill for
679 recycling gangue and controlling strata: creep experiments and models. *Environ Sci Pollut R* 2021
680 <https://doi.org/10.1007/s11356-021-12944-4>
- 681 Xu WB, Zhang YL, Liu B (2020) Influence of silica fume and low curing temperature on mechanical
682 property of cemented paste backfill. *Constr Build Mater* 254:119305.
683 <https://doi.org/10.1016/j.conbuildmat.2020.119305>
- 684 Yilmaz E, Belem T, Benzaazou M (2014) Effects of curing and stress conditions on hydromechanical,
685 geotechnical and geochemical properties of cemented paste backfill. *Eng Geol* 168:23-37.
686 <https://doi.org/10.1016/j.enggeo.2013.10.024>
- 687 Yin DW, Chen SJ, Sun XZ, Jiang N (2021) Effects of interface angles on properties of rock-cemented
688 coal gangue-fly ash backfill bi-materials. *Geomech Eng* 24: 81-89
689 <https://doi.org/10.12989/gae.2021.24.1.081>
- 690 Yin SH, Shao YJ, Wu AX, Wang ZY, Yang LH (2020) Assessment of expansion and strength properties
691 of sulfidic cemented paste backfill cored from deep underground stopes. *Constr Build Mater*
692 230:116983. <https://doi.org/10.1016/j.conbuildmat.2019.116983>
- 693 Zhang XG, Lin J, Liu JX, Li F, Pang ZZ (2017) Investigation of Hydraulic-Mechanical Properties of
694 Paste Backfill Containing Coal Gangue-Fly Ash and Its Application in an Underground Coal Mine.
695 *Energies* 10(9):19. <https://doi.org/10.3390/en10091309>
- 696 Zhu WB, Xu JM, Xu JL, Chen DY, Shi JX (2017) Pier-column backfill mining technology for
697 controlling surface subsidence. *Int J Rock Mech Min* 96:58-65.
698 <https://doi.org/10.1016/j.ijrmmms.2017.04.014>

Figures

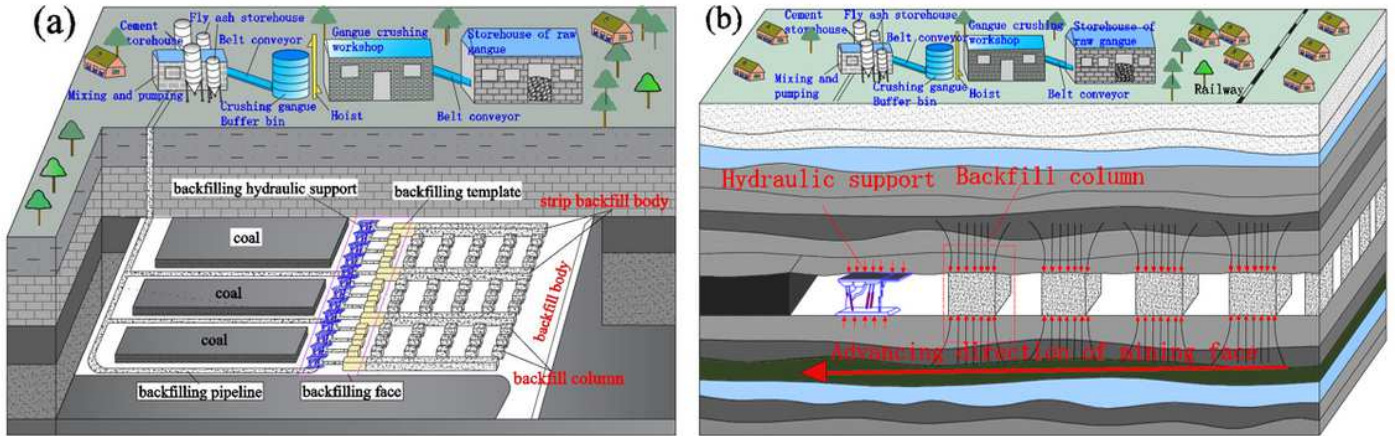


Figure 1

Schematic diagram of the unconfined backfill columns in constructional backfill mining: (a) layout of the unconfined backfill column, (b) load on the unconfined backfill column.

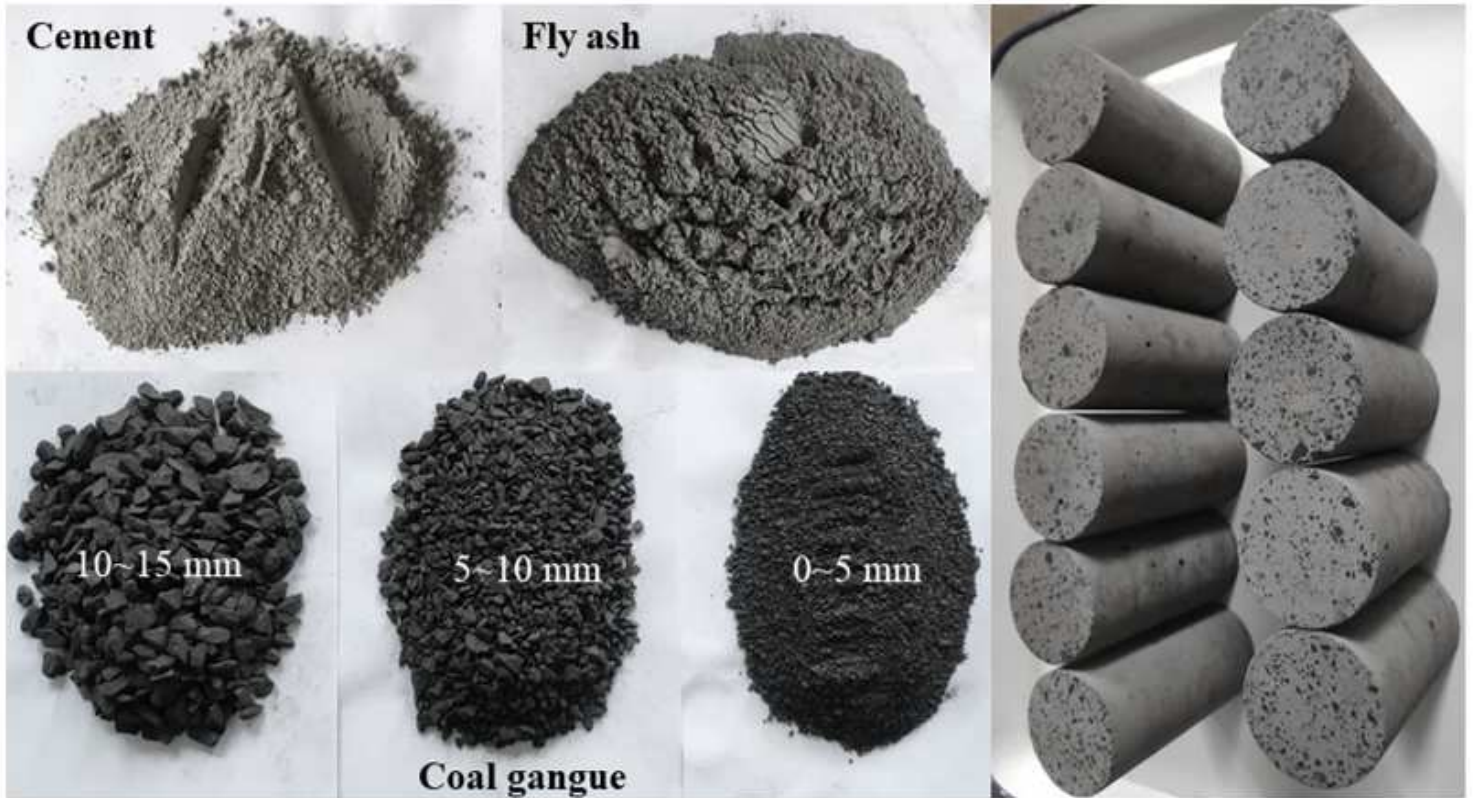


Figure 2

Morphology of raw material and test samples.

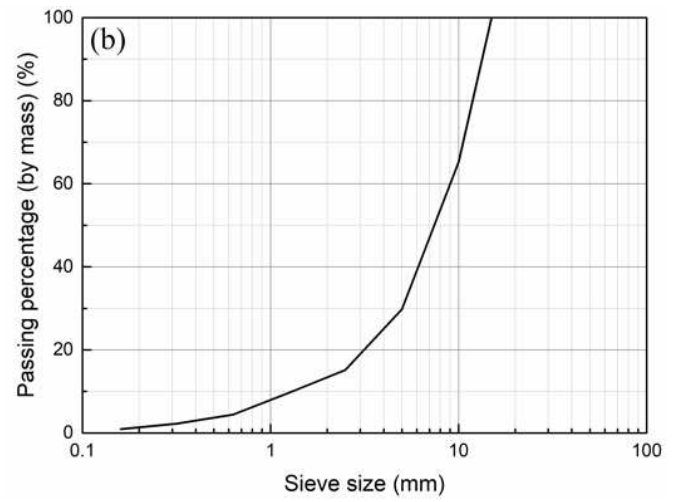
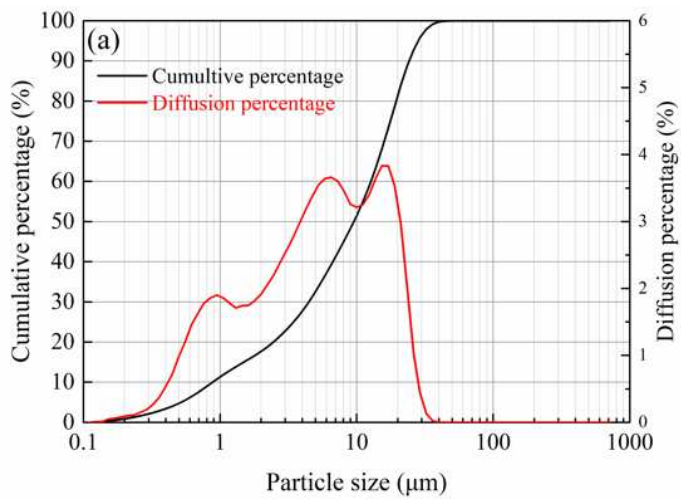


Figure 3

Particle size distribution of fly ash (a) and coal gangue aggregate (b).

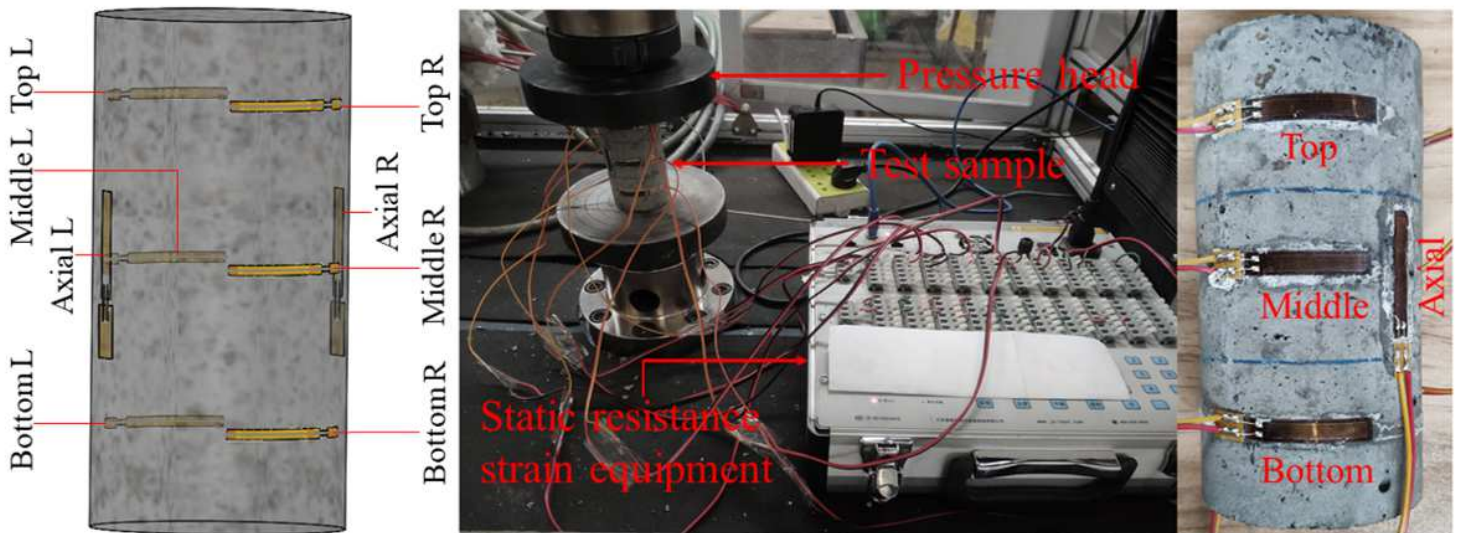


Figure 4

Testing machine and the distribution of strain gauges.

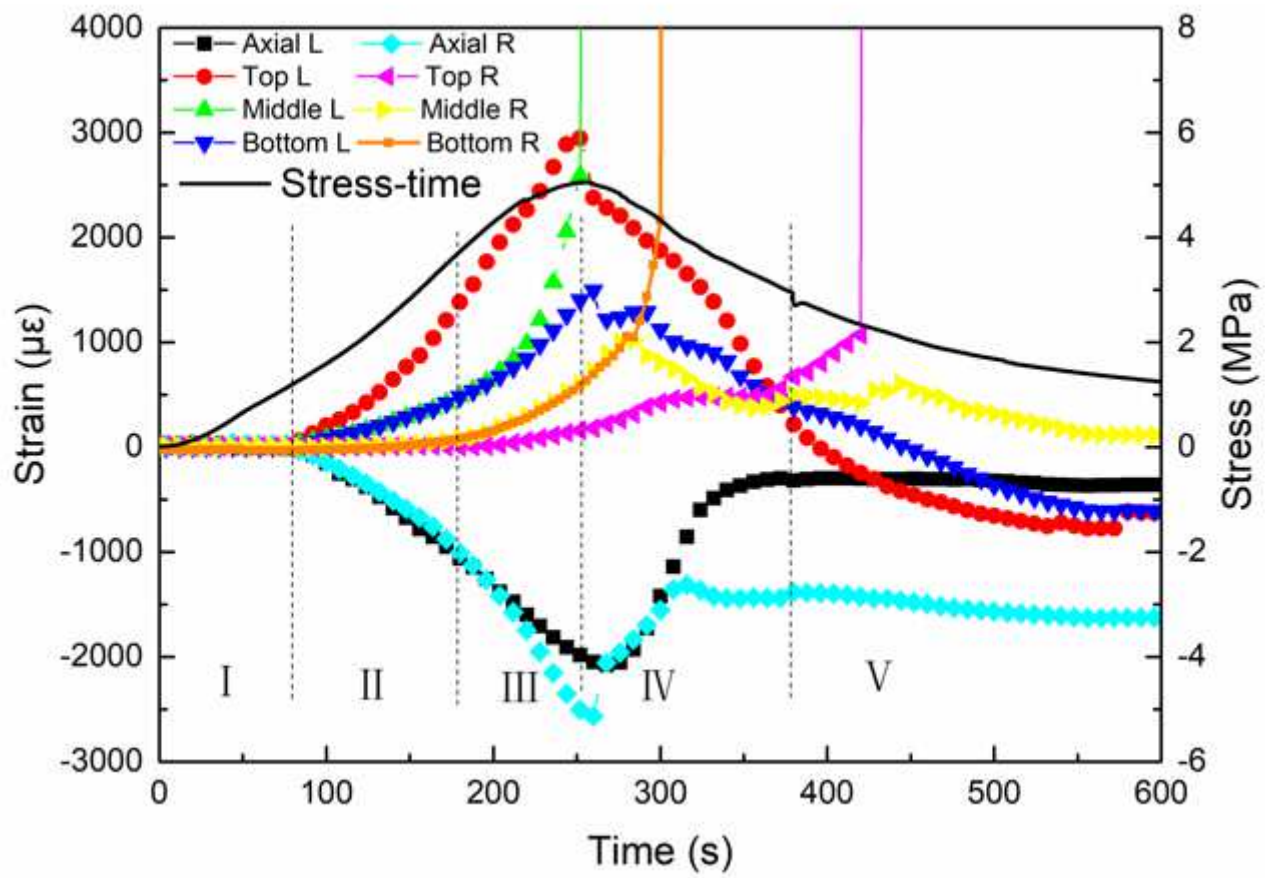


Figure 5

Strain-time curve and stress-time curve under uniaxial compression.

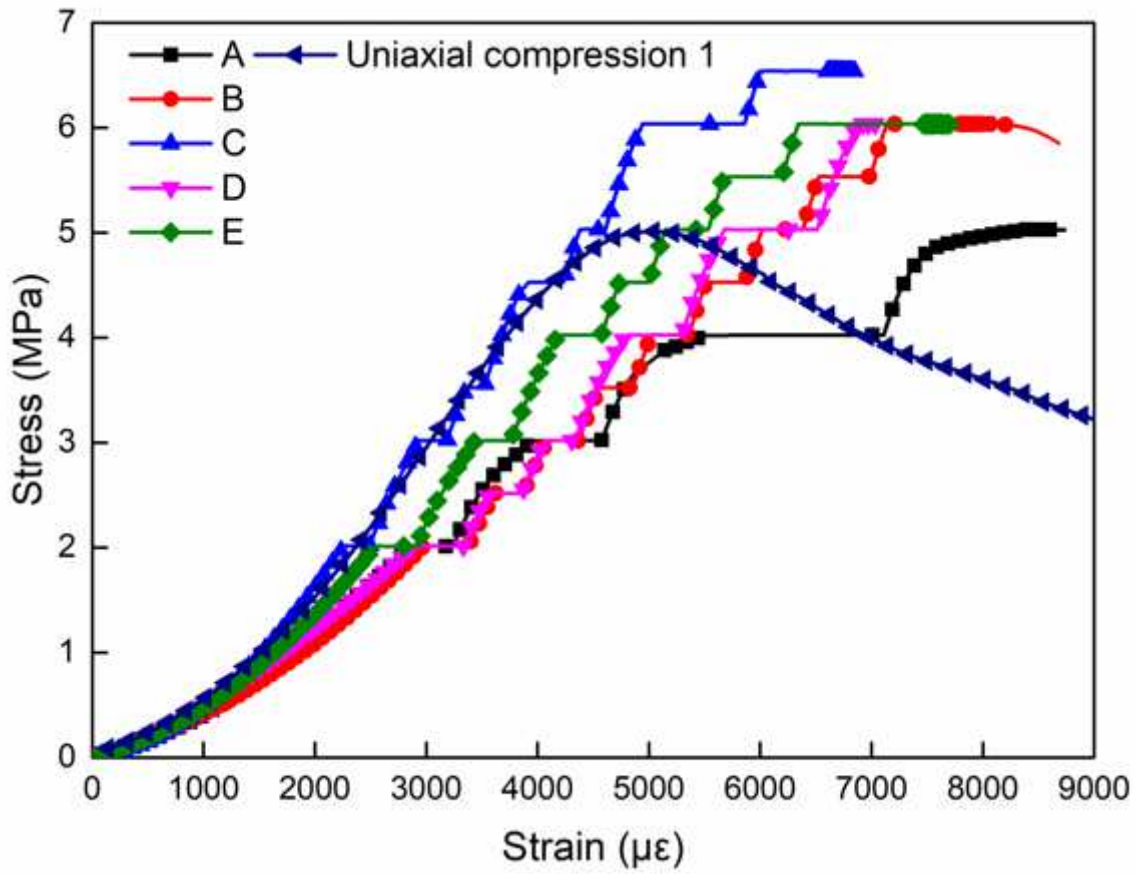


Figure 6

Stress-strain curve under step-by-step load and uniaxial compression.

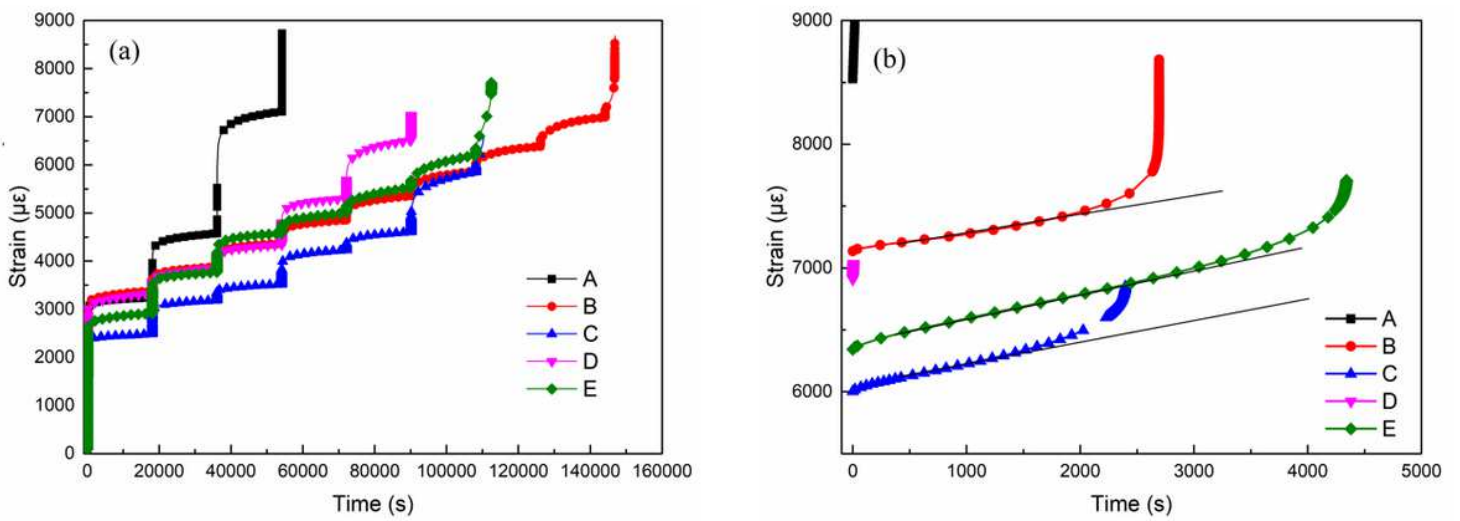


Figure 7

(a) Strain-time curve under step-by-step load. (b) Strain-time curve during the creep instability process.

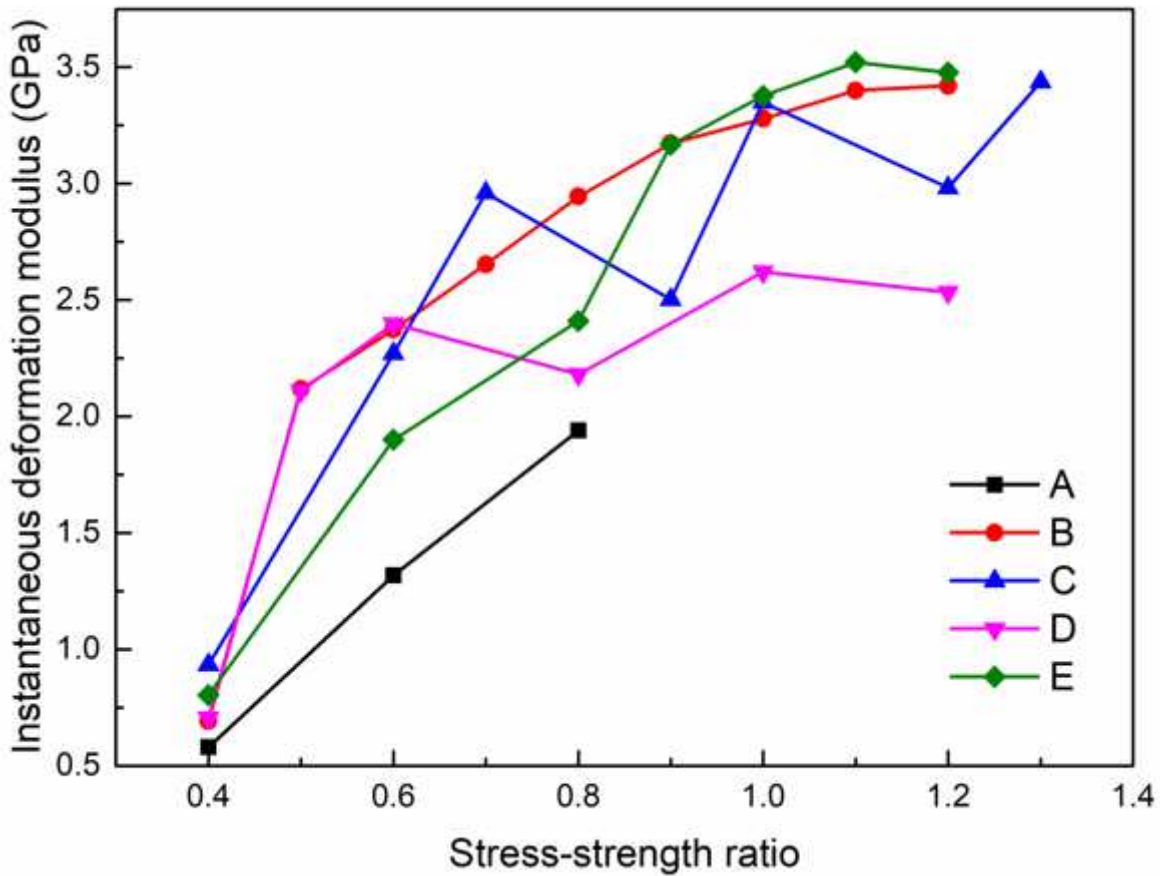


Figure 8

Development of instantaneous deformation modulus.

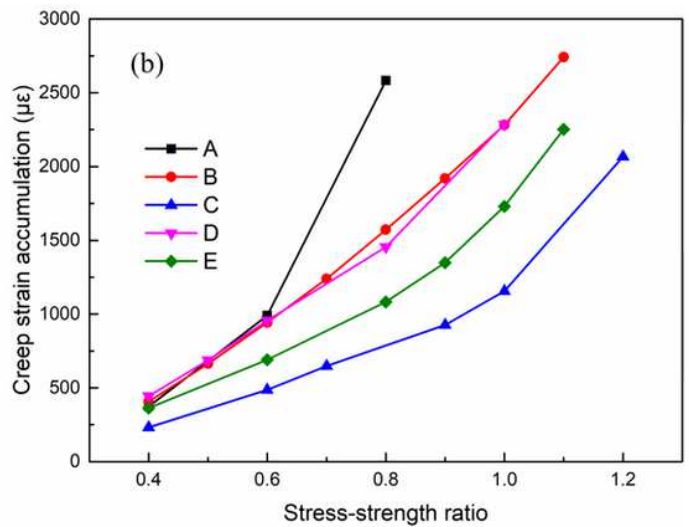
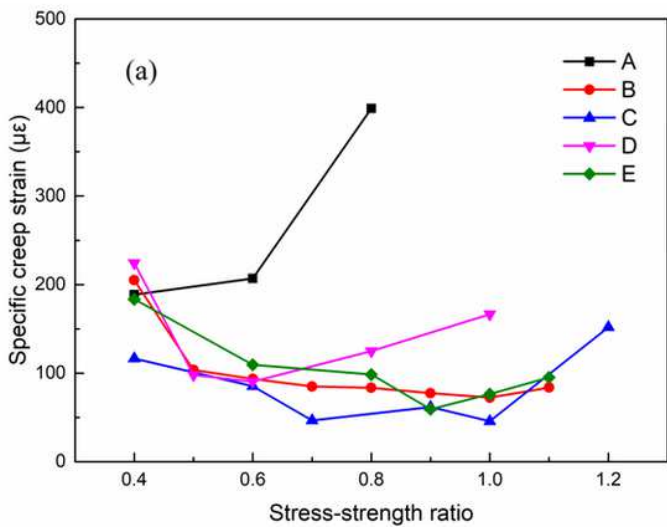


Figure 9

(a) Specific creep strain at different stress–strength ratios; (b) Accumulation of creep strain.

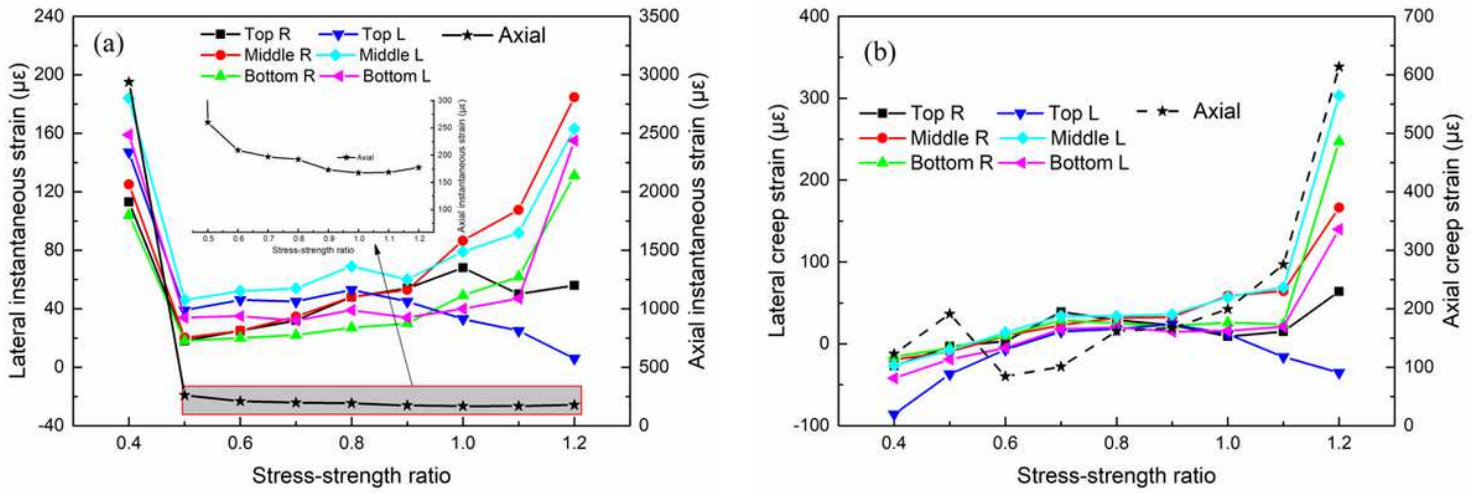


Figure 10

Development of (a) instantaneous strain and (b) creep strain of group B under step-by-step load.

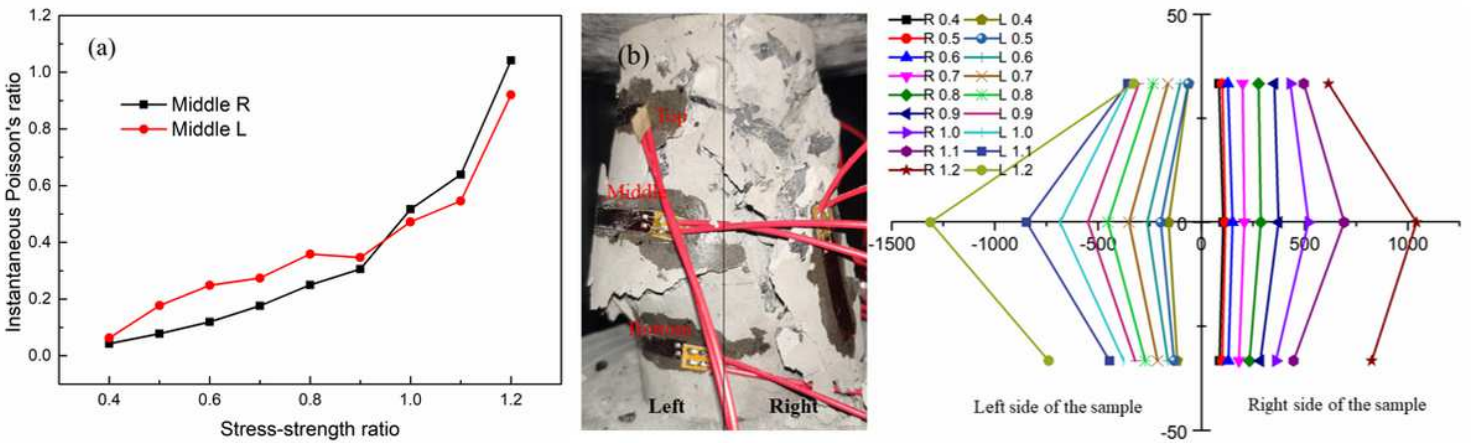


Figure 11

(a) Curve of instantaneous Poisson's ratio; (b) Accumulation of the lateral strain of sample B.

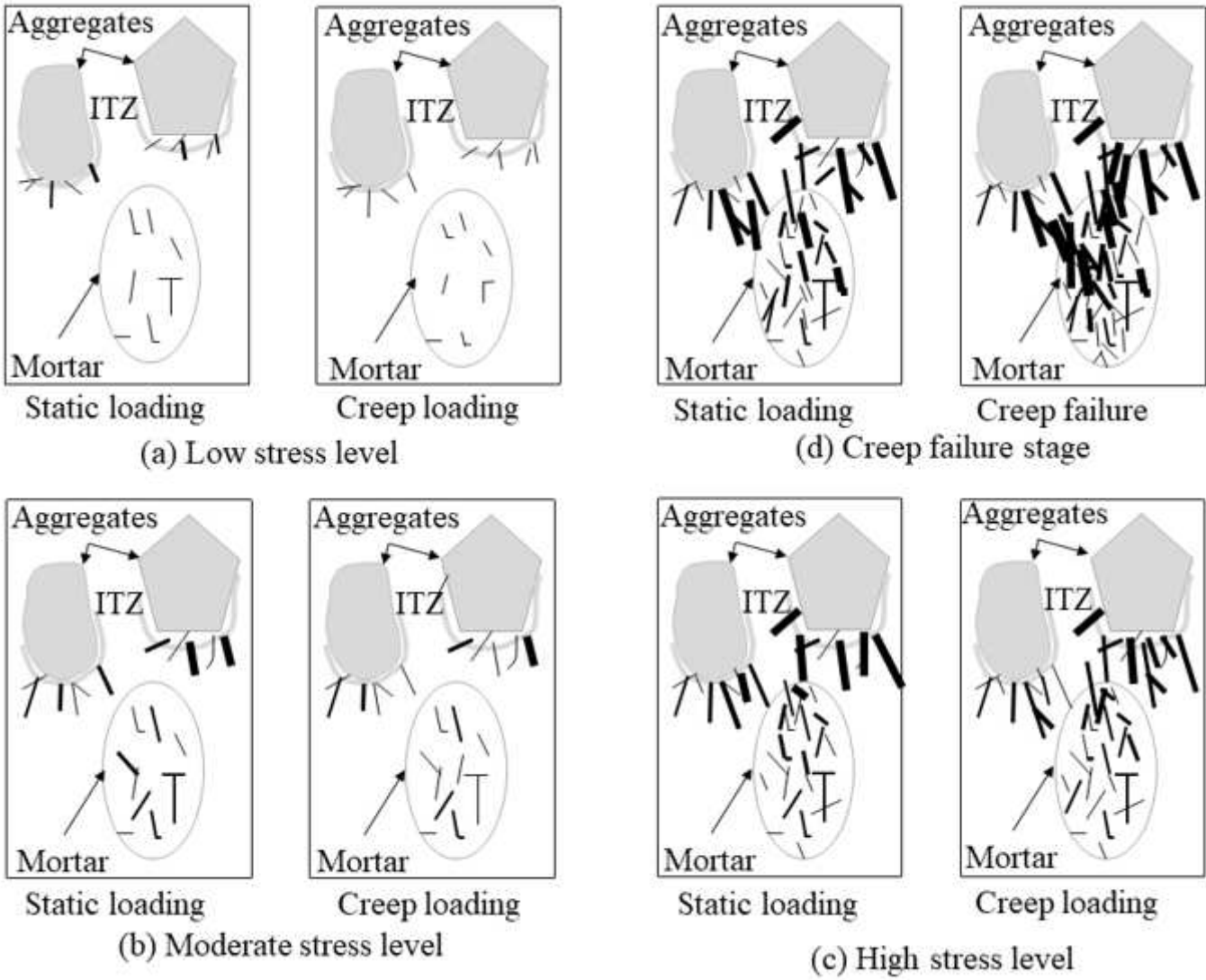


Figure 12

Schematic description of the production of cracks and cracking processes.

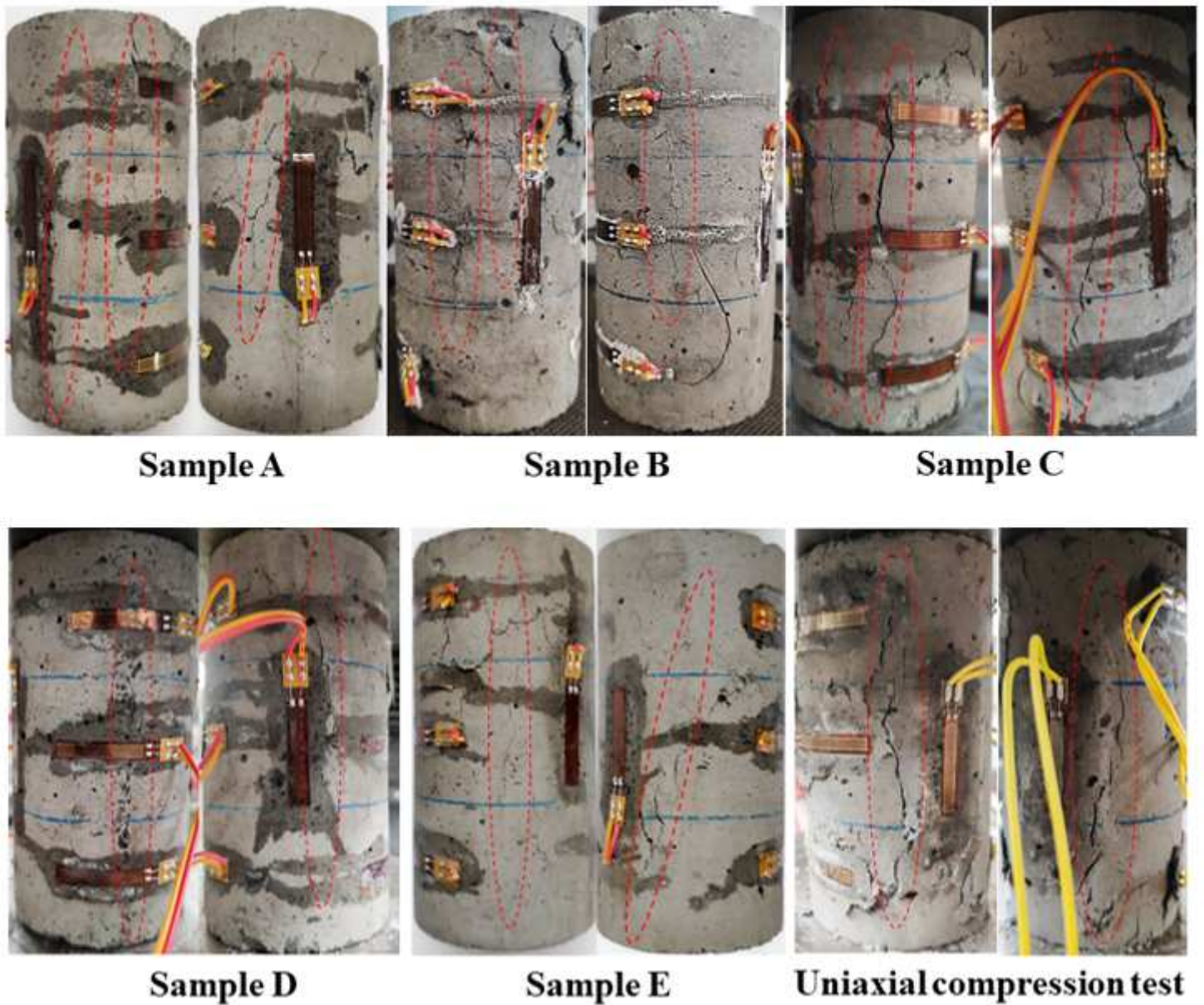


Figure 13

Failure forms of the CGBM samples.

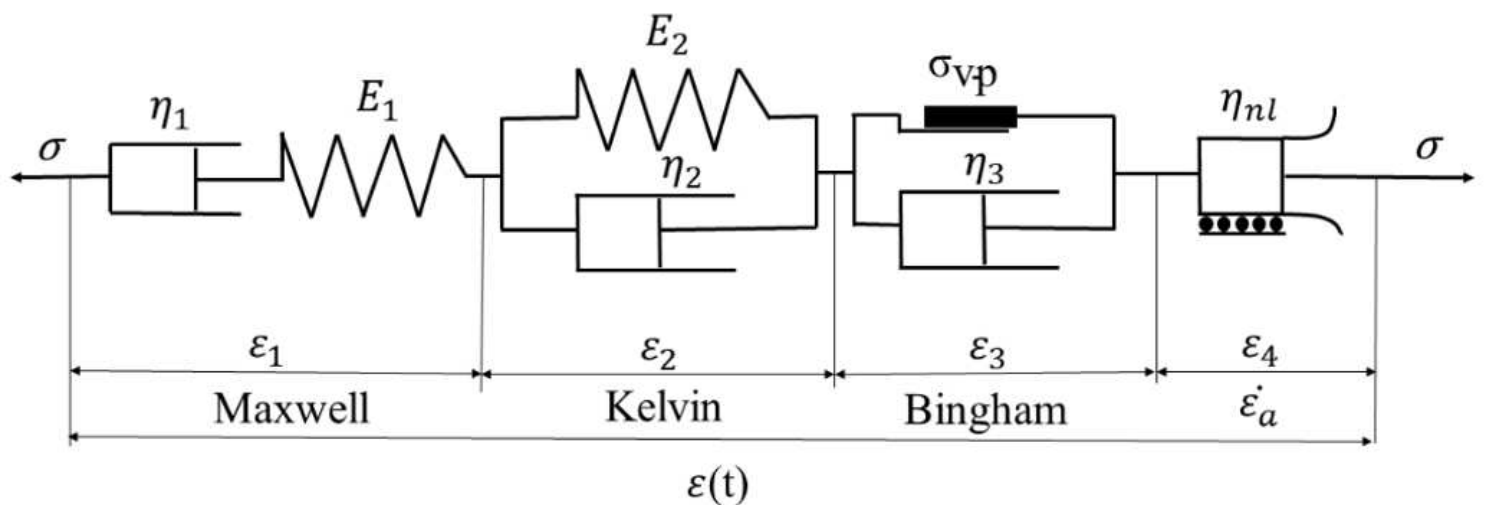


Figure 14

Modified viscoelastic-plastic model for the creep of CGBM.

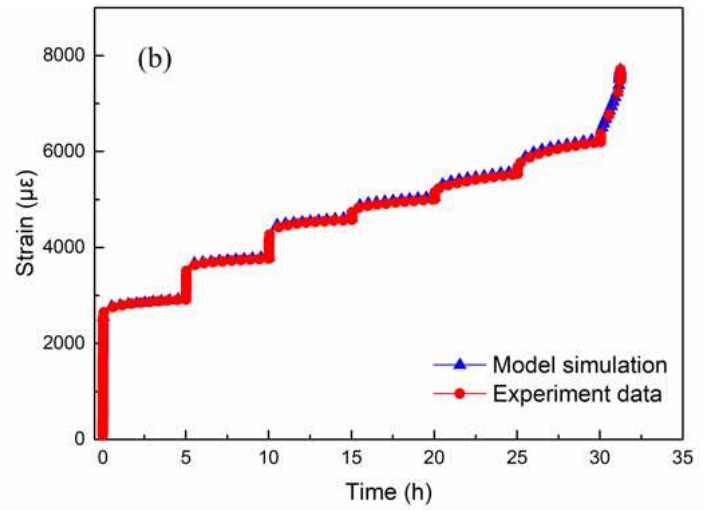
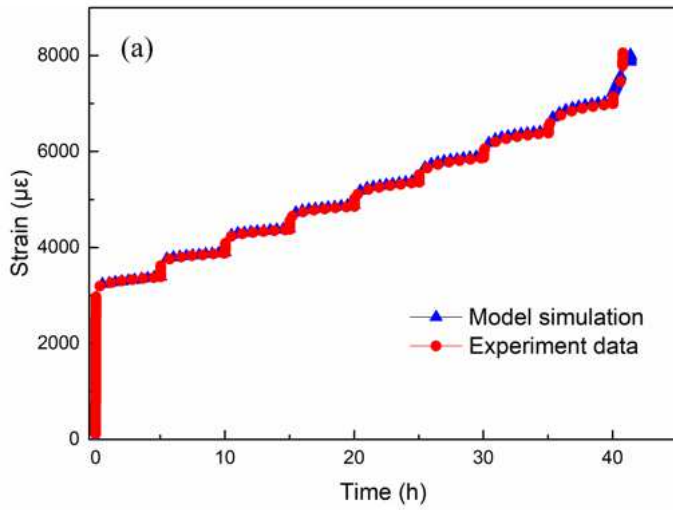


Figure 15

Comparison of the experimental and simulation results of samples (a) B and (b) E.